

# Measuring the non-thermal pressure in early type galaxy atmospheres: A comparison of X-ray and optical potential profiles in M87 and NGC1399

E. Churazov,<sup>1,2</sup> W. Forman,<sup>3</sup> A. Vikhlinin,<sup>3,2</sup> S. Tremaine,<sup>4</sup> O. Gerhard,<sup>5</sup> C. Jones<sup>3</sup>

<sup>1</sup> *Max-Planck-Institut für Astrophysik, Karl-Schwarzschild-Strasse 1, 85741 Garching, Germany*

<sup>2</sup> *Space Research Institute (IKI), Profsoyuznaya 84/32, Moscow 117810, Russia*

<sup>3</sup> *Harvard-Smithsonian Center for Astrophysics, 60 Garden St., Cambridge, MA 02138, USA*

<sup>4</sup> *Institute for Advanced Study, Einstein Dr., Princeton, NJ 08540, USA*

<sup>5</sup> *MPI für Extraterrestrische Physik, P.O.Box 1603, 85740 Garching, Germany*

23 October 2018

## ABSTRACT

We compare the gravitational potential profiles of the elliptical galaxies NGC 4486 (M87) and NGC 1399 (the central galaxy in the Fornax cluster) derived from X-ray and optical data. This comparison suggests that the combined contribution of cosmic rays, magnetic fields and micro-turbulence to the pressure is  $\sim 10\%$  of the gas thermal pressure in the cores of NGC 1399 and M87, although the uncertainties in our model assumptions (e.g., spherical symmetry) are sufficiently large that the contribution could be consistent with zero. In the absence of any other form of non-thermal pressure support, these upper bounds translate into upper limits on the magnetic field of  $\sim 10\text{--}20 \mu\text{G}$  at a distance of  $1'\text{--}2'$  from the centers of NGC1399 and M87. We show that these results are consistent with the current paradigm of cool cluster cores, based on the assumption that AGN activity regulates the thermal state of the gas by injecting energy into the intra-cluster medium. The limit of  $\sim 10\text{--}20\%$  on the energy density in the form of relativistic protons applies not only to the current state of the gas, but essentially to the entire history of the intra-cluster medium, provided that cosmic ray protons evolve adiabatically and that their spatial diffusion is suppressed.

**Key words:**

## 1 INTRODUCTION

Both optical and X-ray data are often used to determine the distribution of the gravitating mass in galaxies. In analysing optical stellar-kinematic data, stars are treated as collisionless particles and the mass distribution is obtained either from the Jeans equations and some assumption about the anisotropy of stellar orbits (Binney & Tremaine 2008; Lokas & Mamon 2003), or by finding the potentials in which a distribution of orbits reproduces the observed surface brightness profile and stellar kinematics (e.g., Kronawitter et al. 2000; Thomas et al. 2007). In X-rays, hydrostatic equilibrium is usually assumed for the gaseous atmosphere and the observed density and temperature distributions are then used to evaluate the distribution of gravitating mass (Mathews 1978; Forman, Jones & Tucker 1985; Fukazawa et al. 2006; Humphrey et al. 2006). Ideally both methods should yield identical results, and the mismatch between gravitating masses derived from optical and X-ray data can be used,

for example, to measure the contribution of non-thermal particles to the gas pressure. Such non-thermal particles are directly observed as bubbles of relativistic plasma (e.g., Boehringer et al. 1993). They can also be present in the ICM due to mixing of thermal and relativistic plasma, or generated by shocks propagating through the ICM. Below we use the newest Chandra data to compare optical and X-ray data in two giant elliptical galaxies. The  $\sim 0''.5$  angular resolution of Chandra has brought the X-ray data on a par with optical data and has made it possible to extend the comparison between the kinematics of stars and hot gas from spatial scales of arcseconds up to  $\sim 10'$  as is done below for two giant elliptical galaxies: M87 and NGC1399.

The fundamental assumption that underlies this paper is that the mass profiles derived from optical observations are correct, so that deviations between the optical and X-ray profiles are due to effects on the gas such as non-thermal pressure. While measuring mass profiles from

stellar-kinematic data involves only gravity and dynamics, uncertainties may remain, mainly because of the degeneracy between radial variations in mass-to-light ratio and radial variations in the anisotropy parameter of the velocity ellipsoid (Binney & Mamon 1982). Breaking this degeneracy is possible when the kinematic data provide sufficient information on higher-order moments of the line-of-sight velocity distribution (LOSVD) and this is used to constrain the distribution of stellar orbits (Gerhard 1993, Merritt 1993). Uncertainties resulting from modeling good quality absorption line spectra are  $\sim 10\%$  in circular velocity over the range of radii covered (e.g., Kronawitter et al. 2000; Thomas et al. 2007, and references therein). Additional reasons to believe that the optical mass profiles that we use in this paper are reliable are: (i) the profiles from M87 and NGC1399 are derived from quite different methods—based on stellar absorption line spectra but including also discrete tracer particles (globular clusters) in the former case—yet yield consistent results for the level of non-thermal pressure; (ii) for both galaxies, the mass distributions have been studied in at least two independent studies that yield consistent results; (iii) most of the concerns about the reliability of optical mass profiles arise from studies with limited observational resolution (e.g., determinations of black-hole masses), limited radial coverage of data, or restrictive modeling techniques (e.g., the assumption of isotropic velocity distributions), neither of which is a concern in the studies used here.

## 2 SELECTION OF M87 AND NGC1399

The choice of M87 and NGC1399 is motivated by the following considerations. We want the objects (i) to be nearly round (E0-E1) elliptical galaxies with existing high quality optical data on stellar kinematics, (ii) to have X-ray emission dominated by diffuse gas, with temperatures not much higher than the velocity dispersion of the galaxy, (iii) to have high-quality Chandra data; (iv) to exhibit at most small or moderate deviations from spherical symmetry in the X-ray images of the hot gas. There are few objects that satisfy all these criteria. For example, condition (i) requires that the object be nearby, while (ii) requires that we study massive early-type galaxies at the center of a group or a cluster with a cool core. Choosing a massive galaxy is necessary to avoid contamination of the X-ray emission by unresolved point sources. For instance in NGC3379 (the dominant elliptical galaxy in the poor Leo group), the X-ray emission remaining after removing bright low mass X-ray binaries has a large (perhaps dominant) contribution from the unresolved stellar population (CVs, coronally active stars). This conclusion follows from the comparison of the unresolved X-ray luminosity per unit K-band optical luminosity of NGC3379 with that for the gas poor bulge of M32 (Revnivtsev et al., 2007, 2008; see also David et al. 2006). Application of the hydrostatic equilibrium equation to such systems would lead to the conclusion that the gas has been heated to a temperature that cannot be bound to the galaxy, and is out-flowing (Pellegrini & Ciotti 2006).

Both M87 and NGC1399 are at least several times more massive than NGC3379. They reside in the gas-rich cool cores of nearby clusters (Virgo and Fornax respectively), and

both objects have excellent optical data and long Chandra observations (see Fig.1,2). Thus, although we plan to apply our technique to additional galaxies in the future, M87 and NGC1399 satisfy all criteria enumerated above and are the best targets for our pilot project.

We assume distances of 16 and 19.8 Mpc for M87 and NGC 1399 respectively.

## 3 OBSERVATIONS AND DATA PREPARATION

Our *Chandra* data analysis is adopted from the reduction procedure described in (Vikhlinin et al. 2005, V05 hereafter). This includes filtering of high background periods and application of the latest calibration corrections to the detected X-ray photons, and determination of the background intensity in each observation.

The quiescent *Chandra* background is dominated by the cosmic X-ray background and charged particle events. The latter component can be subtracted exquisitely accurately (with a  $\lesssim 2\%$  scatter, see Hickox & Markevitch 2006) if one removes the secular trends in background intensity using the hard X-ray band data. The cosmic X-ray background component is modeled adequately by using the “blank-sky” background datasets<sup>1</sup> which include both the particle-induced and unresolved sky components.

The spectral calibration includes removal of the time-dependent gain variations of the ACIS CCDs, and also the most recent corrections for all positional-dependent variations in the ACIS response and effective area. For the discussion of associated uncertainties, see V05. They are negligible for our purposes.

### 3.1 M87 data

For the analysis we used Chandra observations (OBSIDs 5826, 5827, 5828, 6186, 7210, 7211, and 7212) taken at a variety of instrument roll angles from February to November 2005 using the ACIS-I detector (CCDs I0-I3) in Very Faint (VF) mode to minimize the background (see Forman et al. 2007 for details).

We reprocessed all observations applying the latest CTI and time-dependent gain calibrations. We performed the usual filtering by grade, excluded bad/hot pixels and columns, removed cosmic ray ‘afterglows’, and applied the VF mode filtering. We also reprocessed two Faint mode ACIS-S OBSIDs (3717 and 2707) and treated the front (S2) and back (S3) illuminated CCDs independently. We compared the images from the Very Faint and Faint mode observations to verify that no artifacts were introduced near the bright jet by the use of the large  $5 \times 5$  pixel event regions in VF mode. We examined the data for background flaring and found moderate flaring in OBSIDs 3717 and 2707 (the back illuminated CCDs only) for which we excluded approximately half the duration. A typical effective exposure time is  $\sim 500$  ksec. The background files (see Markevitch 2001 for details) were processed in exactly the same manner as the observations.

<sup>1</sup> See <http://cxc.harvard.edu/contrib/maxim>

During 41 ms of the 3.2 s nominal exposure readout of the ACIS CCDs, the chips are exposed to the sky. This results in a small contribution of the source flux, 1.3%, being uniformly re-distributed along the readout direction. This ‘readout artifact’ is most clearly visible when there is a bright point source in the FOV which produces a characteristic readout streak. However, for any emission where a bright region contaminates one of lower surface brightness, this effect must be taken into account. The readout artifact can be accurately subtracted using the technique described by Markevitch et al. (2000). A new event file is generated using the original data by randomizing the CHIPY-coordinate and all sky coordinates and energies are recalculated as if it were a normal observation. The new event file is renormalized by the ratio of the readout time compared to the integration time (41 ms/3.2 s = 0.013) and then treated exactly as another component of the background. The blank-field background is also renormalized by reducing its integration time by 1.3% to account for this additional subtraction. The M87 nucleus and the brightest jet knot were piled-up in most of the observations and the corresponding readout streaks were completely excluded from the analysis.

As the last step of data preparation, an additional column was added to each event list. For a given event in the list this column  $\eta$  contains the ratio of the effective area for a photon with a given energy at a given position  $A(E, x_d, y_d)$  to a predefined function of energy  $A_0(E)$ :

$$\eta = A(E, x_d, y_d)/A_0(E), \quad (1)$$

where  $A(E, x_d, y_d)$  includes mirror and detector efficiencies (including non-uniformity of the detector quantum efficiency and the time and spatially dependent contamination on the optical blocking filter). Our data set largely consists of ACIS-I data and a natural choice is to set  $A_0(E)$  to the ACIS-I on-axis effective area. This makes  $\eta$  equal to the vignetting of the mirrors, modified by the (energy dependent) variations of quantum efficiency across the detector. The same procedure was repeated with the background data. Finally, for each event list, we make an exposure map that accounts for all position dependent, but energy independent, efficiency variations across the focal plane (e.g., overall chip geometry, dead pixels or rows, variation of telescope pointing direction).

### 3.2 NGC 1399 data

For NGC 1399 we used Chandra data of OBSIDs 319, 4172 and 4174, having a total useful exposure of  $\sim 120$  ksec. The data were cleaned and processed using the same procedures as for the M87 data.

## 4 DEPROJECTION

We use the observations from M87 to describe our method in detail and to explore biases arising from multi-temperature gas components. Such components are clearly visible in M87 (see Fig. 1) and are less prominent in NGC 1399 (see Fig. 2). Hence, M87 provides the most stringent test of our method.

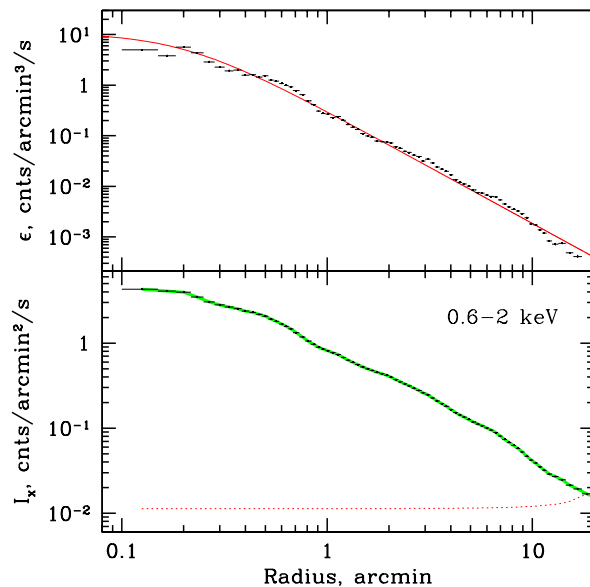


**Figure 3.** M87 surface brightness in the 0.6–2 keV band (lower panel) and the emissivity profile in the same band (upper panel). The solid line in the upper panel shows the function  $(1 + (r/r_c)2)^{-3\beta}$ , with  $\beta = 0.37$  and  $r_c = 0.2'$ . Clearly, the  $\beta$ -model provides a reasonable, but not perfect, description of the gas emissivity in the 0.6–2 keV band. The thick green line in the lower panel shows the projection of the emissivity profile for comparison with the observed surface brightness. It goes through the data points, showing that the deprojection solution is exact. The nearly horizontal dotted line is the contribution to the surface brightness in each annulus from the outer gas layers (outside  $19'$ ), where the gas emissivity is assumed to decline as a power law of radius.

### 4.1 Broad band

First, using the event lists for all 9 observations, we build an image in the 0.6–2 keV band, centered at the M87 nucleus,  $40'$  on a side and with  $1''$  pixels. To build this image, the image pixels were initialized to zero, then for each event in the event list with energy in this range, we added the value  $1/\eta$  to the corresponding image pixel<sup>2</sup>. The same procedure was applied to the background event lists. An exposure map was generated combining exposure maps for individual event lists. A background-corrected surface brightness profile  $S_{obs}(i)$  calculated from the ‘ $1/\eta$ ’ image in a set of annuli centered at the M87 nucleus is shown in the bottom panel of Fig. 3. The surface brightness is normalized to counts per arcmin<sup>2</sup> per second.

In our deprojection analysis, we follow the approach used in Churazov et al. (2003) (see Appendix A for addi-

<sup>2</sup> Since  $\eta$  is essentially the vignetting factor (relative to the on-axis position), populating images with  $1/\eta$  instead of 1 for each event is equivalent to applying the vignetting correction during image construction instead of accounting for this factor in the exposure map. The logic behind this approach is further discussed in Section 4.2.

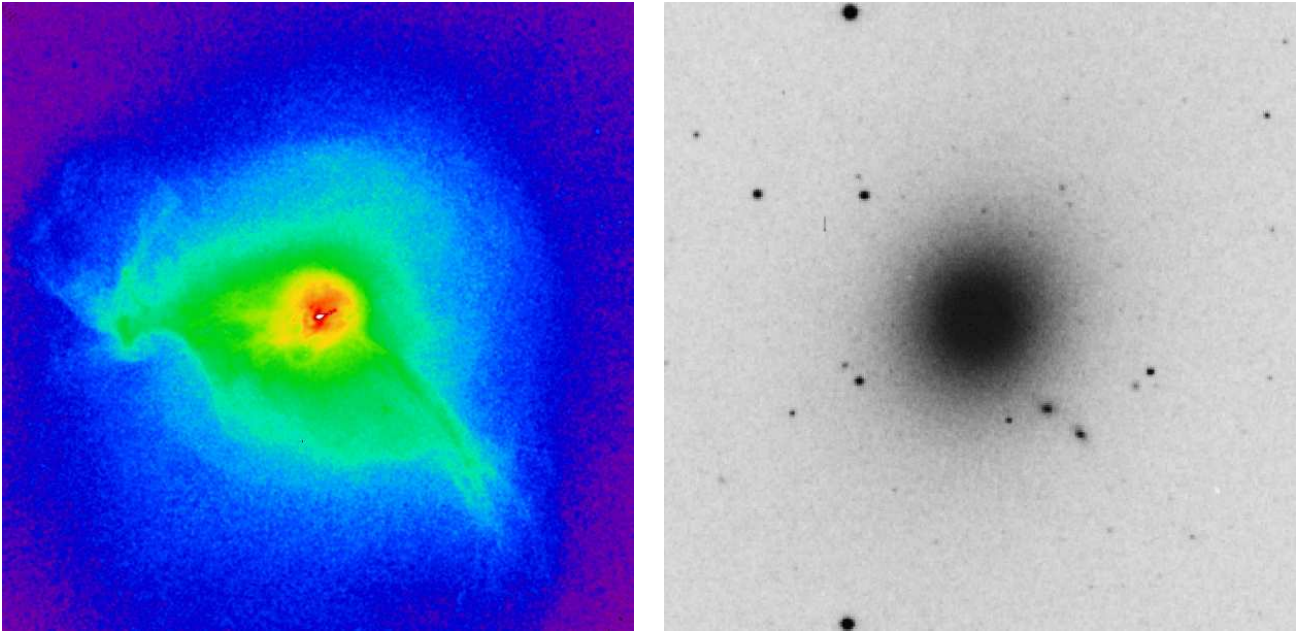


**Figure 1.** Central  $10' \times 10'$  ( $10' = 47$  kpc) region of the Chandra 0.6–2 keV (left) and DSS optical image (right) of M87. The galaxy appearance is very regular in the optical band, while the X-ray image is moderately disturbed. In these and other images throughout the paper, north is up and east is to the left.

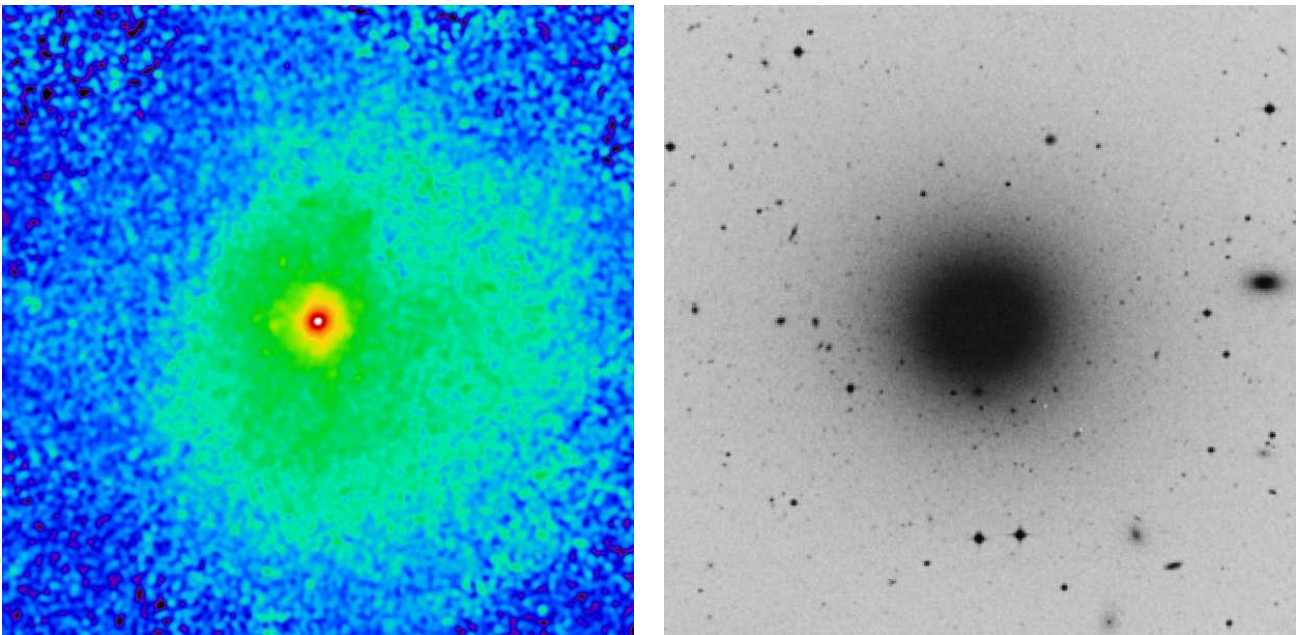


**Figure 2.** Central  $10' \times 10'$  ( $10' = 58$  kpc) region of the Chandra 0.6–2 keV (left) and DSS optical image (right) of NGC1399. As for M87, the optical galaxy is very regular, while the X-ray image shows only moderate deviations from spherical symmetry and appears considerably less disturbed than M87.

tional discussion). We assume spherical symmetry, but make no specific assumption about the form of the underlying gravitational potential. For a given surface brightness profile in  $n_a$  annuli, we choose a set of  $n_s$  ( $n_s \leq n_a$ ) spherical shells with the inner radii  $r(i)$ ,  $i = 1, \dots, n_s$ . The gas emissivity  $\mathcal{E}$  is assumed to be uniform inside each shell, except for the outermost shell, where the gas emissivity is assumed to decline as a power law of radius:  $\mathcal{E} = \mathcal{E}_{out} r^{-6\beta_{out}}$ , where

$\beta_{out}$  is a parameter. In our analysis  $r(n_s)$  was set to  $19'$  and  $\beta_{out} = 1/3$ . In practice, we are mostly working with the data inside a  $10'$  circle and the precise values of  $\beta_{out}$  and the outer radius do not affect the results.

The expected surface brightness can then be written as a projection of emissivities in each of the  $n_s - 1$  shells plus

a contribution from the outer layers ( $r > r(n_s)$ ):

$$S(j) = \sum_{i=1}^{n_s-1} P(i, j) \mathcal{E}(i) + P_{out}(j) \mathcal{E}_{out}, \quad (2)$$

where  $\mathcal{E}(i)$  is the emissivity of a given shell,  $\mathcal{E}_{out}$  is the emissivity of the outer layers of the gas at  $r = 1$ , and  $P(i, j)$  and  $P_{out}(j)$  are the projection matrix/vector from our set of shells into our set of annuli. A simple analytical expression for  $P(i, j)$ , which is a function of the geometry only, is given by McLaughlin (1999).

Deprojection can then be reduced to a simple least squares problem – what set of emissivities in our set of shells (together with the emissivity normalization  $\mathcal{E}_{out}$  for the outer layers) provides the best description of the observed surface brightness:

$$\chi^2 = \sum_j [S(j) - S_{obs}(j)]^2 / \sigma(j)^2 = \min \quad (3)$$

where  $\sigma(j)$  is the error associated with the surface brightness in annulus  $j$ . In our analysis, we use modified errors  $\sigma(j)^2 = \sigma_{stat}(j)^2 + \delta^2 \times S_{obs}^2(j)$ , where  $\sigma_{stat}(j)$  is the statistical error associated with the Poisson noise in the observed image and background and  $\delta \sim 0.1$ . This was done to avoid the situation where a few annuli with the best statistics completely dominate the  $\chi^2$ . In practice for the M87 dataset, the choice of  $\delta$  does not affect the results. As usual the differentiation of this relation with respect to  $\mathcal{E}(i)$  and  $\mathcal{E}_{out}$  yields a system of linear equations  $\tilde{P}\mathcal{E} = \tilde{S}$ , which can easily be solved. Here  $\tilde{P}$  is the square  $n_s \times n_s$  matrix and each of the  $n_s$  elements of  $\tilde{S}$  vector are the linear combinations of the original observed values of  $S_{obs}$ . In the cases considered below, the solution of equation (3) is unique, once the parameter  $\beta_{out}$  is fixed. The properties of the inverse matrix  $\tilde{P}^{-1}$  (in particular an error enhancement when the ratio of maximal to minimal eigenvalues of  $\tilde{P}$  is large) can easily be controlled by making the spherical shells broader. A practical recipe for the choice of shells/annuli radii will be described elsewhere.

The emissivity of each shell can then be evaluated as an explicit linear combination of the observed quantities:

$$\mathcal{E}(i), \mathcal{E}_{out} = \sum_{j=1, n_s} \tilde{P}^{-1}(j, i) \tilde{S}(j) = \sum_{j=1, n_a} D(j, i) S_{obs}(j), \quad (4)$$

where  $D$  is the final  $n_a \times n_s$  deprojection matrix relating the observed surface brightness in rings and the emissivities of spherical shells. Since the whole procedure is linear, the errors in the observed quantities can be propagated straightforwardly. Shown in Fig. 3 (upper panel) is the set of gas emissivities in the 0.6–2 keV band derived from the surface brightness profile. The forward convolution of this set of emissivities with the projected matrix  $P(i, j)$  (green line in the lower panel of Fig. 3) exactly reproduces the observed surface brightness profile.

## 4.2 Deprojected spectra

Note that with our definition of  $\eta$ , the projection matrix  $P(i, j)$  does not depend on energy. Indeed all energy/position dependent factors are already corrected for when we make the  $1/\eta$  image instead of a usual image constructed from raw counts without any weights. We do lose some of the sensitivity with this  $1/\eta$  procedure, but very

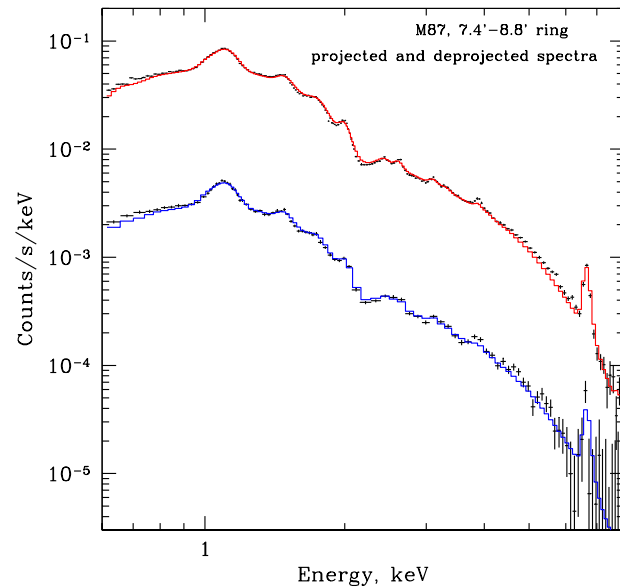


**Figure 4.** Projected (top) and deprojected (bottom) spectra for the 7.4–8.8 annulus/shell in M87 (black crosses) together with the best fitting single-temperature APEC model (red and blue histograms). The best fitting temperatures are 2.57 and 2.4 keV for projected and deprojected spectra respectively. Both spectra are reasonably well described by a single temperature APEC model.

little as long as the variations of  $1/\eta$  across the region used for spectrum extraction are not large. Note that since the exposure time is dominated by that from the ACIS-I chips, the factor  $\eta$  is a smooth function of energy and our  $1/\eta$  technique does not introduce spurious spectral features.

Since  $P(i, j)$  does not depend on energy, the deprojection of a surface brightness profile in any energy band would look like equation (4) with exactly the same  $D(j, i)$ . Thus we can accumulate a set of ‘ $1/\eta$ ’ spectra (corrected for background and readout) for each of the  $n_a$  annuli, and apply equation (4) to determine the emissivities of each shell in each of the ACIS energy channels. We note here that a similar technique of vignetting correction at the level of individual events is often used in the analysis of X-ray data (e.g. for XMM-Newton). For M87 Chandra observations we explicitly verified that fitting of ‘ $1/\eta$ ’ and ‘regular’ spectra of the same regions yields fully consistent results.

The procedure described above differs slightly from the often used onion peeling algorithm or `project` in XSPEC (Arnaud 1996). A short note on the different deprojection techniques is given in the Appendix A. The bottom line is that all techniques should yield consistent results if underlying assumptions are correct. Our procedure is computationally fast and is especially useful when a large number of spherical shells are analyzed.

The resulting spectra were fitted in XSPEC V12 (Arnaud 1996) with a single-temperature optically thin plasma emission model as implemented in the APEC code (Smith et al. 2001). The low energy photoabsorption was fixed at

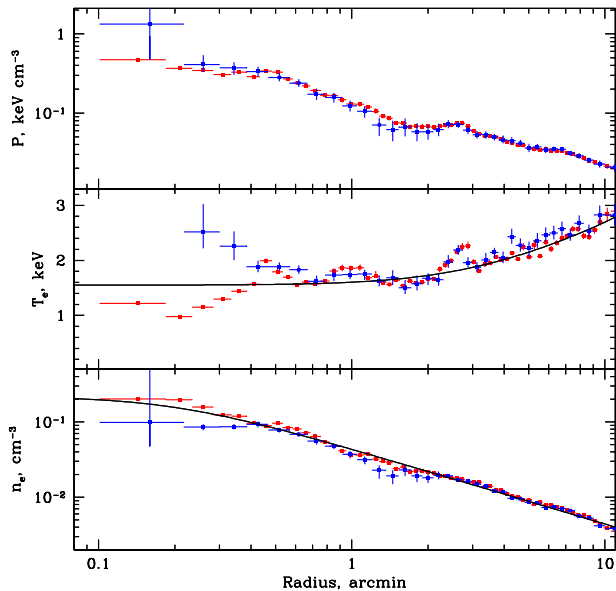


**Figure 5.** Radial profiles of deprojected gas parameters in M87. The parameters were obtained using a single temperature APEC model (with fixed low energy absorption and redshift) fit to the deprojected spectra for a set of spherical shells centered on M87. The red and blue points correspond to the best-fitting parameters for the 0.6–9 keV and 2.5–9 keV energy bands respectively. Simple analytical approximations for the density and temperature are shown with the solid lines (eqs. 6 and 7). The uppermost panel shows the gas pressure evaluated as  $P = nT = 1.91n_eT_e$ , where  $n_e$  and  $T_e$  are the best-fitting electron density and temperature. Outside the central 0'.4 the best fit parameters for the two bands agree well, suggesting that the impact of multi-temperature plasma on the  $n_e$  and  $T_e$  is not strong.

the Galactic value  $N_H = 2.54 \times 10^{20} \text{ cm}^{-2}$  (Dickey & Lockman 1990) and the redshift was fixed at the optically determined redshift of M87:  $z = 0.00436$  (e.g., Smith et al. 2000). The gas temperature, heavy metal abundance and normalization were free parameters of the model. A sample spectrum in the 7'.4 – 8'.8 annulus and the deprojected spectrum in the spherical shell of the same size are shown in Fig. 4 together with the best fitting single-temperature APEC model. The best fitting temperatures are 2.57 and 2.4 keV for projected and deprojected spectra respectively. The deprojected spectra were generated in narrow (14.6 eV) energy bins and used in XSPEC without any further grouping. To avoid a bias towards lower temperatures, which is present when the number of counts per spectral bin at high energies becomes less than  $\sim 10 - 20$ , the statistical errors were evaluated from the smoothed spectra, while the fitting is applied to raw (unsmoothed) spectra (see Churazov et al. 1996 for details). This approach suppresses the bias associated with the low number of counts per spectral bin provided that total number of counts in the spectrum is large. We did verify earlier for ASCA (Churazov et al. 1996) and XMM-Newton data and now for Chandra observations of M87 that this approach yields fully consistent results to an often used technique of grouping spectral channels in bins with at least

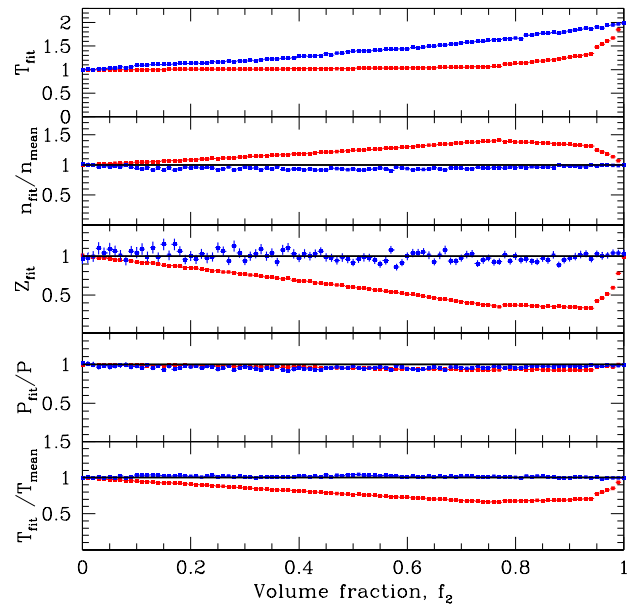


**Figure 6.** ‘Biases’ in a two-temperature plasma versus volume fraction of the hotter component. Fake Chandra spectra representing a mixture of  $kT_1 = 1$  and  $kT_2 = 2$  keV plasmas in pressure equilibrium were fitted with a one-temperature model in the 0.6–9 and 2.5–9 keV bands (red and blue points respectively). The five panels from top to bottom show i) the best-fitting gas temperature, ii) the ratio of best-fitting gas density to the true mean density, iii) gas metallicity, iv) gas pressure  $P_{fit} \equiv n_{fit}T_{fit}$ , v) the ratio of the measured value  $P_{fit}/n_{fit} \equiv T_{fit}$  to the true value  $P/n_{mean} \equiv T_{mean}$ ; here  $n_{mean}$  is the volume averaged plasma density (eq. 5). The last quantity characterizes the bias in measuring the gravitating mass or the potential from the hydrostatic equilibrium equation.

10–20 counts (assuming that the correct spectral model is used). Note that we also verified that allowing the Fe abundance to vary separately from the  $\alpha$ -elements altered the fits by not more than the statistical errors.

The electron density was derived from the normalization of the spectra, fixing the proton to electron ratio to 0.83 and taking into account the distance to M87. The resulting spectral parameters are plotted in Fig. 5 as a function of distance from the center of M87. Red and blue points correspond to the best-fitting model parameters in the 0.6–9 and 2.5–9 keV bands respectively. This choice of two energy bands for spectral fitting is motivated on the following grounds: the broader band maximizes the statistical significance of the results, while the harder band provides a verification of the magnitude of biases which might arise when a one-temperature model is applied to a spectrum with multiple temperature components (e.g., Buote 2000).

To assess the magnitude of possible biases when fitting the multi-temperature plasma in the Chandra band with a one-temperature model, we generated a sequence of fake spectra representing a mixture of  $kT_1 = 1$  and  $kT_2 = 2$  keV plasmas in pressure equilibrium, with a varying volume fraction  $f_2$  of the harder component. These two temperatures are characteristic for multi-temperature plasma in the inner

parts of M87 and NGC1399 (Buote 2002). The abundance of heavy elements was set to solar for both components, and  $N_H$  and redshift were fixed to the M87 values. The on-axis ACIS-I response was used. We then applied to the simulated spectra the same one-temperature model as we did for the real M87 data. The resulting spectral parameters are shown in Fig. 6: temperature, density, metallicity, pressure  $P_{fit} \equiv n_{fit}T_{fit}$ , and the ratio of the measured value  $P_{fit}/n_{fit} \equiv T_{fit}$  to the true value  $P/n_{mean} \equiv T_{mean}$ ;

$$n_{mean} = n_1 \times (1 - f_2) + n_2 \times f_2 \quad (5)$$

is the volume averaged plasma density and  $n_1$  and  $n_2$  are the plasma densities of the cooler and hotter phases respectively (evaluated as 1.91 times the respective electron densities  $n_e$ ). The quantity  $T_{fit}/T_{mean} - 1$  characterizes the bias in measuring gravitating mass or potential from the hydrostatic equilibrium equation. The red and blue points correspond to the best-fitting parameters derived from the 0.6–9 and 2.5–9 keV bands respectively. For the 0.6–9 keV band, even a very small volume fraction of the cooler component causes the best-fitting temperature and metallicity to drop sharply, while the density rises (red points in Fig. 6). For the 2.5–9 keV band, the density is, on the contrary, very close to the mean value. This conclusion is of course sensitive to the particular choice of  $T_1$  and  $T_2$  and to the effective area of the instrument. In general, one expects the best-fitting temperature in the broad band to be more biased towards lower values compared to the hard band. It is possible therefore to use the differences in the best-fitting values obtained in two energy bands as an indicator of strong departures from a single-temperature plasma. From Fig. 5 it is clear that the best-fitting values in the 0.6–9 and 2.5–9 keV bands differ strongly inside the inner  $0'.4$ , while outside this radius, the results agree well. Of course even a reasonable agreement between the spectral results in two bands does not guarantee that the spectrum is fully described by a one-temperature model. This agreement nevertheless suggests that outside  $0'.4$  our spectral results are not strongly biased. On the other hand, the region inside  $0'.4$  is characterized by very strong departures from spherical symmetry and by the presence of cool and hot gas structures. Given the magnitude of the expected biases the results for this region should be taken with caution.

From Chandra and XMM-Newton observations we know that the gas temperature in the X-ray bright features co-spatial with the extended radio bright ‘arms’ is lower than that of the typical intra-cluster medium (ICM) temperature at the same distance from the center (e.g., Belsole et al. 2001; Matsushita et al. 2002; Forman et al. 2005). These regions are clearly seen in Fig. 7, where the 0.6–2 keV image of M87 is divided by an axisymmetric  $\beta$ -model, as extended structures to the east and the south-west of the nucleus. To test whether these structures dramatically affect our final result (e.g., the mass/potential profile, discussed below) we also fit the data excluding those regions containing the brightest parts of the arms. We use the spectral fits to this ‘trimmed’ data-set in the next section to verify the robustness of our results.

Analytical approximations to the best-fitting values of  $n_e(r)$  and  $kT(r)$  over the range of radii from  $\sim 0.5'$  to  $\sim 10'$

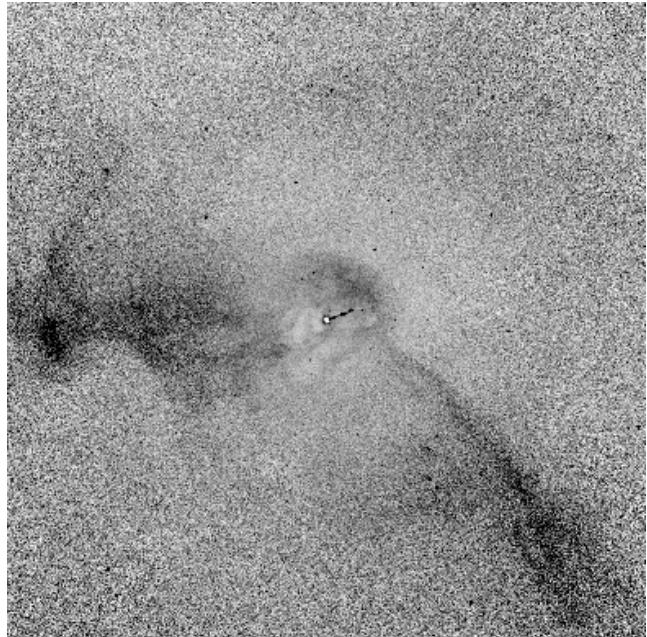


**Figure 7.** Central  $10' \times 10'$  part of the 0.6–2 keV image of M87, divided by the axisymmetric model with surface brightness  $I(R) \propto (1 + (R/r_c)^2)^{1/2-3\beta}$  (here  $R$  is the distance from the M87 nucleus,  $\beta = 0.37$  and  $r_c = 0.2'$ ) to show the structure in the surface brightness more clearly.

are given below:

$$n_e = 0.22 \left[ 1 + \left( \frac{r}{r_c} \right)^2 \right]^{-\frac{3}{2}\beta} \text{ cm}^{-3}, \quad (6)$$

where  $\beta = 0.33$  and  $r_c = 0.2'$  (or 0.93 kpc).

$$kT = 1.55 \times \left[ 1 + \left( \frac{r}{2.2'} \right)^2 \right]^{0.18} \text{ keV}. \quad (7)$$

These approximations are shown in Fig. 5 by the black solid lines.

## 5 POTENTIAL

We first derive the gravitational potential for M87, including a detailed discussion of the method which we then apply to the data for NGC 1399.

### 5.1 M87

We assume that the gaseous atmosphere of M87 is in hydrostatic equilibrium:

$$\frac{1}{\rho} \frac{dP}{dr} = -\frac{d\varphi}{dr} \quad (8)$$

where  $\rho$  is the gas density,  $P = P(r)$  is the pressure and  $\varphi$  is the gravitational potential. Thus

$$\varphi = - \int \frac{1}{\rho} \frac{dP}{dr} dr \quad (9)$$

If the pressure is solely due to the thermal gas pressure, then  $P = nkT$  and  $\rho = \mu m_p n$ , where  $\mu$  is the mean atomic weight

of the gas particles,  $m_p$  is the proton mass, and  $n = n(r)$  is the total particle density. Then (assuming that  $\mu$  does not vary with radius) the potential  $\varphi$  is:

$$\varphi = -\frac{k}{\mu m_p} \left[ \int T \frac{d \ln n}{dr} dr + T \right] + C \quad (10)$$

where  $C$  is an arbitrary constant. Below we will use the value of the potential relative to a given reference radius  $r_{ref} = 5'.5$  (25.6 kpc), i.e.,  $\varphi(5'.5) = 0$ . Note that eq. (10) depends only on the measured quantities  $n(r)$  and  $T(r)$ . Furthermore, eq. (10) does not depend explicitly on radius  $r$  (only through  $n(r)$  and  $T(r)$ ) or on the absolute normalization of the gas density. This in particular means that the assumed distance to M87 does not affect the calculated potential as long as it is expressed as a function of angular distance from the nucleus. Thus  $\varphi$  can be easily evaluated using the densities and temperatures derived from the deprojected X-ray spectra. Unlike the expression for gravitating mass, which explicitly depends on the spatial derivatives of the observed quantities, the change of the potential  $\Delta\varphi$  between two radii  $r_1$  and  $r_2$  depends primarily on the gas densities at two radii and on the mean gas temperature. For example, in the case of isothermal gas,  $\Delta\varphi \propto T \ln [n(r_2)/n(r_1)]$  which is of course a direct consequence of the Boltzmann distribution. This makes the calculation of  $\Delta\varphi$  very simple and robust.

Below we will denote the potential derived from X-ray data (by means of eq. 10) as  $\varphi_X$  to distinguish it from the true potential  $\varphi$  or from the potential  $\varphi_{opt}$  derived from optical data.

Note that the derived spectral parameters in each bin are not independent random variables since they come from the deprojection analysis, e.g., the emissivities in the spherical shells are various linear combinations of the same set of original independent data points (fluxes in the concentric annuli around the source). For a given spherical shell the errors are evaluated correctly since the spectrum is calculated as an explicit linear combination of independent variables. However, it is expected that the deviations from the correct values in nearby radial shells are correlated/anti-correlated. Thus, if we repeat the same observation many times, the measured values of the emissivity will lie within the estimated uncertainties in 67% of cases (apart from possible systematic errors), but the values in nearby radial bins may change in correlated/anti-correlated ways.

Similarly, the values of  $\varphi_X$  obtained at different radii are not statistically independent, both because they are derived from the deprojected spectral parameters and because the value of  $\varphi_X$  at each radius depends on the same set of spectral parameters in various radial bins according to equation (10). Rigorous error calculations would require error propagation from the original (independent) spectra obtained in the set of annuli around the source; these would be difficult to do and the results would be difficult to present simply. However, in practice we believe this more rigorous analysis may be replaced with a straightforward error calculation. Indeed, for the case of an isothermal gas  $\varphi_X(r) = \frac{k}{\mu m_p} T \ln n(r) + C$ , i.e.,  $\varphi_X(r)$  depends only on the local (at radius  $r$ ) gas density. Therefore, the error distribution for  $\varphi_X(r)$ , at any given radius  $r$ , can be correctly estimated, as long as the errors in  $n(r)$  are correct (see previous paragraph). The same is approximately true for a slowly

**Table 1.** Data used to derive the potential.

Regions	Energy band	Color in Fig. 8
0-360° annuli	0.6–9 keV	blue
0-360° annuli, excluding ‘arms’	0.6–9 keV	red
0-360° annuli, excluding ‘arms’	2.5–9 keV	green

varying temperature profile. Below, we assign to each  $\varphi_X(r)$  the error which follows from equation (10, assuming that the errors in evaluating the spectral parameters at each radius are independent.

In Fig. 8 we show three versions of  $\varphi_X$  derived from the Chandra data for M87. Each of the three shaded ‘curves’ corresponds to different subsets of data and/or different energy bands used for spectral fitting, as indicated in Table 1. The regions that exclude ‘arms’ are described more fully at the end of §4.2. The vertical width of each of the color curves in Fig. 8 corresponds to the 67% statistical uncertainty.

All three methods lead to estimates of  $\varphi_X(r)$  that are consistent with each other within statistical uncertainties. The potential derived from the data in the 2.5–9 keV band has the largest statistical errors, but as discussed above, the spectral parameters may be less biased in this band, compared to the broader 0.6–9 keV band. We note here that departures from spherical symmetry are obvious from Fig. 1 and we cannot expect the spectral parameters (or potential profiles) to be perfectly consistent with each other.

For comparison to the X-ray derived gravitational potentials, we show in Fig. 8, with the black lines, two estimates of the gravitational potential that are derived from the optical data. The dashed line shows the potential derived by Wu & Tremaine (2006, their §4.3.2; WT06 below) using a sample of 161 globular clusters in M87. The mass profile in this model is a power law function of radius  $M(r) = 2.3 \times 10^{10} M_\odot (r/\text{kpc})^{1.36}$ . This mass distribution is most accurately determined near  $r = 30$  kpc, but Wu & Tremaine estimate that the relative error in  $M(r)$  is less than 40% for  $17 \text{ kpc} < r < 90 \text{ kpc}$  (or  $3.7' < r < 19'$ ). The error in the potential is substantially smaller, since it is determined by the integral of the mass distribution,  $\phi_{opt} = \int_{r_{ref}}^r GM(r) dr/r^2$ . The potential in the inner few arcminutes is only weakly constrained since this model does not use any information on stellar kinematics. The thick solid (black) line in Fig. 8 is the best-fitting model to the star and globular-cluster kinematics in M87 from Romanowsky & Kochanek (2001, see their §4.2; hereafter, RK01). This model (NFW2 in their Table 2) has a mass profile that is the sum of an NFW profile (Navarro, Frenk & White, 1996) from a dark halo and a stellar component, derived from the M87 optical surface brightness under the assumption of a constant stellar mass-to-light ratio. In terms of the likelihood, this is the most probable model among those considered by RK01. This model agrees reasonably well with the X-ray derived potential apart from a few clear wiggles in  $\varphi_X(r)$ , which we discuss in Section 6.5. Two other models – NFW1 and NFW3 (see Table 2 of RK01) are shown in Fig. 8 with the thin solid lines. In terms of likelihood/significance these models are  $\sim 0.8$  and  $0.9 \sigma$  “dispreferred” compared to the best fitting NFW2 model. The difference between these



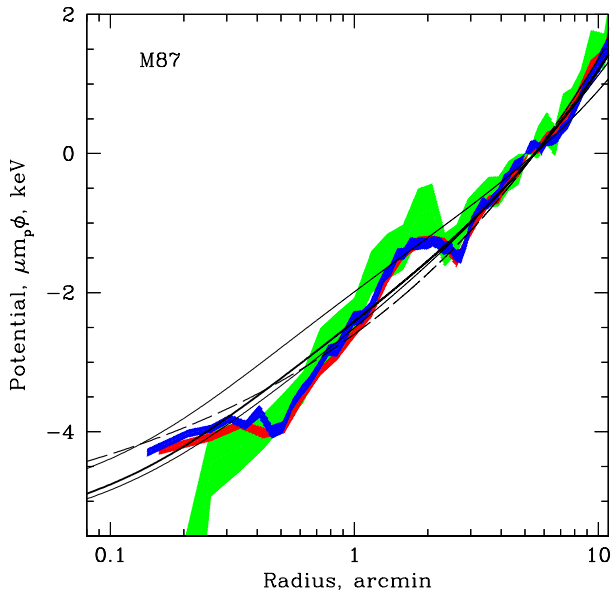


**Figure 8.** Derived potential  $\varphi_X(r)$  using the 0.6–9 keV band (blue), the same excluding ‘cool arms’ (red), the same in the 2.5–9 keV band (green) – see Table 1. Black curves - potentials  $\varphi_{opt}(r)$  derived from the optical data: Wu & Tremaine (2006) - dashed line; Romanowsky & Kochanek (2001), NFW2 model - thick solid line. The comparison of the thick black and colored curves suggests that  $\varphi_{opt}(r)$  and  $\varphi_X(r)$  broadly agree over the range of radii shown in the figure. Thin solid lines are the models NFW1 and NFW3 from RK01 which in terms of likelihood/significance are  $\sim 0.8$  and  $0.9 \sigma$  “dispreferred” compared to the best fitting NFW2 model. The difference between these curves approximately characterizes the uncertainties in  $\varphi_{opt}(r)$  based on the analysis of RK01. All curves are normalized to zero at  $5'.5$  radius.

curves can be used to approximately characterize the uncertainties in  $\varphi_{opt}(r)$  based on the parametric model of RK01.

We use below the power law model of WT06 and the NFW2 model of RK01 as two versions of  $\varphi_{opt}(r)$  and assume that the difference between these two models is comparable to the deviations of either from these models from true potential of the galaxy.

## 5.2 NGC 1399

The X-ray potential  $\varphi_X(r)$  derived from Chandra data for NGC 1399 is shown in Fig. 9 with the blue curve. The potential is set to zero at  $1'.5$ . In X-rays the core of NGC 1399 appears less disturbed than M87 and the resulting  $\varphi_X(r)$  is much smoother than for M87. For comparison  $\varphi_{opt}(r)$  based on the model of Kronawitter et al. (2000) is shown with the black solid line, and their  $2\sigma$  confidence bands as the thin black lines. As in the case of M87, there is good agreement of  $\varphi_X(r)$  and  $\varphi_{opt}(r)$  over the region where X-ray and optical data are available.

The optical potential  $\phi_{opt}$  for NGC 1399 was derived from absorption-line kinematic data, as described in Saglia et al. (2000). These authors constructed spherical models for the galaxy in a sequence of gravitational potentials, com-

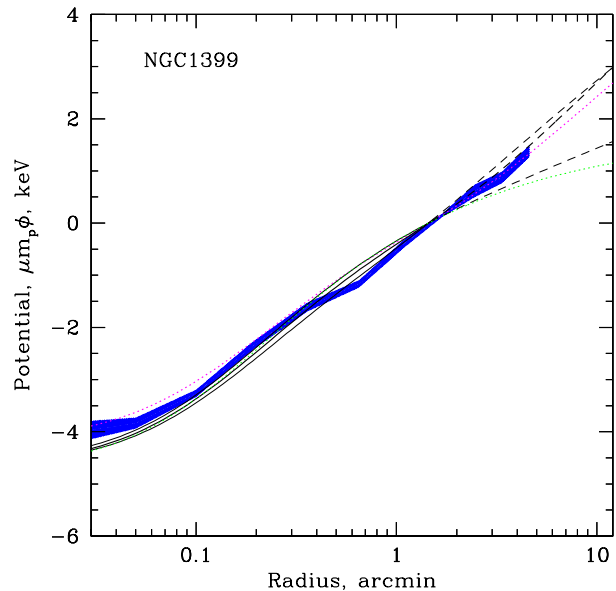


**Figure 9.** Derived potential  $\varphi_X(r)$  for NGC 1399 using the 0.6–9 keV band for  $0-360^\circ$  annuli (blue curve). The thick black solid line shows the potential  $\varphi_{opt}(r)$  derived from optical data of Kronawitter et al. (2000), while thin black lines show  $\pm 2\sigma$  limits. Outside the range of radii covered by the optical data ( $r < 1.62'$ ), the extrapolation of the potential is shown by dashed lines. The green curve is the ‘stars-only’ model from Kronawitter et al. (2000). The magenta line shows the optical potential  $\varphi_{opt}(r)$  multiplied by 0.9. All curves are normalized to zero at  $1'.5$ . The good agreement of  $\varphi_{opt}(r)$  and  $\varphi_X(r)$  suggests that the fraction of non-thermal pressure is low.

posed of the potential of the luminous stars and various optional quasi-isothermal dark halo potentials. The potential of the stars was based on the deprojected luminosity distribution and the assumption of constant mass-to-light ratio. For each of these potentials, the non-parametric distribution function  $f(E, L^2)$ , that gave the best fit to the kinematic data (velocity dispersion and symmetric  $4^{th}$  moment  $h_4$  of the LOSVD), was found; here  $E$  and  $L$  denote energy and total angular momentum. The  $\Delta\chi^2$  values of the various models then determined the boundaries of the confidence region for the halo potential parameters. Similar models, based on a larger basis of distribution functions and potentials, were constructed by Kronawitter et al. (2000). The Kronawitter et al. models are plotted in Fig. 9 and span the 95% confidence range within their expanded set of potentials. The true confidence range based on non-parametric potentials is likely to be somewhat larger; however, it is not straightforward to determine. An independent investigation by Graham et al. (1998) yields similar results.

## 6 EFFECTS OF MAGNETIC FIELDS, COSMIC RAYS, AND MICRO-TURBULENCE

The good agreement between the gravitational potentials derived independently from the optical and X-ray data,

found in the previous section, suggests that hydrostatic equilibrium is satisfied reasonably well in M87 and NGC1399. This conclusion contrasts with that of Diehl & Statler (2007) who have argued recently that hydrostatic equilibrium of the X-ray gas in elliptical galaxies is “the exception rather than the rule” and “X-ray-derived radial mass profiles may be in error by factors of order unity”. In particular, NGC1399 is one of the objects from the Diehl & Statler (2007) sample that is identified as being far from hydrostatic equilibrium based on differences in the isophotal shapes of the stars and the X-ray gas. We believe that the close agreement of the potential profiles  $\phi_X(r)$  and  $\phi_{opt}(r)$  obtained in the previous section would be an improbable coincidence if hydrostatic equilibrium were not approximately valid. While neither NGC1399 nor M87 are in perfect equilibrium, as indicated by visibly disturbed X-ray images (see e.g. Buote & Tsai, 1995), the estimate of the magnitude of the departure from hydrostatic equilibrium by Diehl & Statler (2007) is too pessimistic. We will further test this statement in a larger sample of elliptical galaxies in future work.

We now consider how magnetic fields, cosmic rays and micro-turbulence would affect the potential  $\varphi_X(r)$  derived from the X-ray data. We keep the hydrostatic equilibrium assumption (eq. 9), but we now allow the pressure or density derived from X-ray analysis to differ from the true  $P$  and  $\rho$  entering eq. (9).

### 6.1 Uniform medium

Let us first keep the assumption that the X-ray emitting gas is uniform within each spherical shell, but assume that this gas provides only part of the total pressure. The rest of the pressure is provided by a component that is ‘invisible’ in X-rays (e.g., cosmic rays), which is also uniformly distributed through the volume of each shell. Here and below we assume (unless stated otherwise) that the pressure is isotropic and the atmosphere is in hydrostatic equilibrium, with the thermal gas ‘mechanically’ coupled to other components. We define the fraction of the pressure due to thermal gas as  $f_g = f_g(r)$ . Then the pressure derived from X-ray data will be  $nkT = f_g P$ , where  $P$  is the true total pressure,  $n$  and  $T$  are the density and temperature measured from X-ray data. If we further assume that only thermal gas contributes to the mass density, then  $\rho = \mu m_p n$  will be correctly determined from the X-ray analysis. The temperature is also assumed to be determined correctly. Substituting  $f_g P$  instead of  $P$  into eq. (9), we can easily express  $\varphi_X(r)$  through the true potential  $\varphi(r)$  and other gas parameters:

$$\varphi_X = \int f_g d\varphi - \frac{k}{\mu m_p} \int T \frac{d \ln f_g}{dr} dr. \quad (11)$$

If  $f_g$  does not depend on radius then obviously  $\varphi_X = f_g \varphi$ .

Shown in Fig. 10 is  $\varphi_X$  from eq. (11) for  $f_g = \text{const} = 0.5$  and 0.85 (magenta solid and dotted lines respectively) and for

$$f_g = [1 + (r/1')^2]/[2 + (r/1')^2] \quad (12)$$

(red dashed line). The latter case illustrates the situation when gas pressure dominates at large radii ( $f_g = 1$ ), but declines to 50% of the total pressure ( $f_g = 0.5$ ) in the core. In these calculations we used  $\varphi$  based on the NFW2 model of RK01 and the analytic approximation of temperature given

by eq. (7). The curves for  $f_g = 1$  and  $f_g = 0.85$  fit the X-ray data reasonably well, while the other models are excluded. For NGC 1399, the  $\varphi_X$  and  $\varphi_{opt}$  closely follow each other. Values of  $f_g$  smaller than 0.9 (dotted magenta line in Fig. 9) would lead to a substantial disagreement between  $\varphi_X$  and  $\varphi_{opt}$  over the range of radii from few arcseconds to  $\sim 2'$ .

### 6.2 Micro-turbulence

If small scale and isotropic turbulent motions are present in the medium, then the impact on  $\varphi_X$  can be evaluated similar to the case considered in the previous section. The quantity  $1 - f_g$  characterizes the contribution of turbulent motions to the pressure (or energy density) of the medium.

### 6.3 Bubbles of relativistic plasma

We now assume that the medium is not uniform. Let  $f_g$  be the volume fraction filled with thermal gas. The remaining volume fraction is completely devoid of thermal gas and is occupied by bubbles of cosmic rays and magnetic fields. Both phases are assumed to be in pressure equilibrium and coupled together. If, in performing the X-ray deprojection, one still assumes that the gas is uniform (as we did above), the derived gas density will be lower than the true gas density in the gas patches and higher than the mean volume density:  $\rho_{obs} = \rho_{gas} \sqrt{f_g} = \rho_{mean} / \sqrt{f_g}$ . The pressure derived from the X-ray analysis will be modified accordingly. For this case, the potential is:

$$\varphi_X = \int f_g d\varphi - \frac{1}{2} \frac{k}{\mu m_p} \int T \frac{d \ln f_g}{dr} dr. \quad (13)$$

The X-ray potential  $\varphi_X$  derived from eq. (13) for  $f_g$  given by eq. (12) is shown in Fig. 10 by the green line.

We note here that a similar problem (the impact of bubbles on the observed gas distribution) has been recently considered in Nusser & Silk (2007).

### 6.4 Summary of the effects of non-thermal pressure components on $\varphi_X(r)$

As discussed above we consider the following forms of non-thermal pressure support as the most relevant: (i) cosmic rays and magnetic fields uniformly mixed with the thermal gas (Section 6.1), (ii) cosmic rays and magnetic fields forming bubbles that are free of thermal gas (Section 6.3) and (iii) micro-turbulence in the thermal gas (Section 6.2). For all these cases non-thermal pressure manifests itself as a coefficient in the relation  $d\varphi_X \approx f_g d\varphi$  if  $f_g$  is independent of radius. For  $f_g$  varying with radius the dependence on  $f_g(r)$  is slightly more complicated (see eqs. 11 and 13), with an additional term in  $\phi_X(r_2) - \phi_X(r_1)$  roughly equal to  $-\frac{kT}{\mu m_p} \ln \frac{f_g(r_2)}{f_g(r_1)}$ , where  $f_g(r_2)$  and  $f_g(r_1)$  are the thermal gas pressure fractions at two radii. Therefore, the comparison of the change of  $\varphi_X$  to the true potential (if it is known) over the broad range of radii from  $r_1$  to  $r_2$  provides a simple and convenient way of estimating  $f_g$ —the contribution of the non-thermal components to the total pressure— independent of the “form” of the non-thermal pressure. This applies also to combinations of micro-turbulence, cosmic

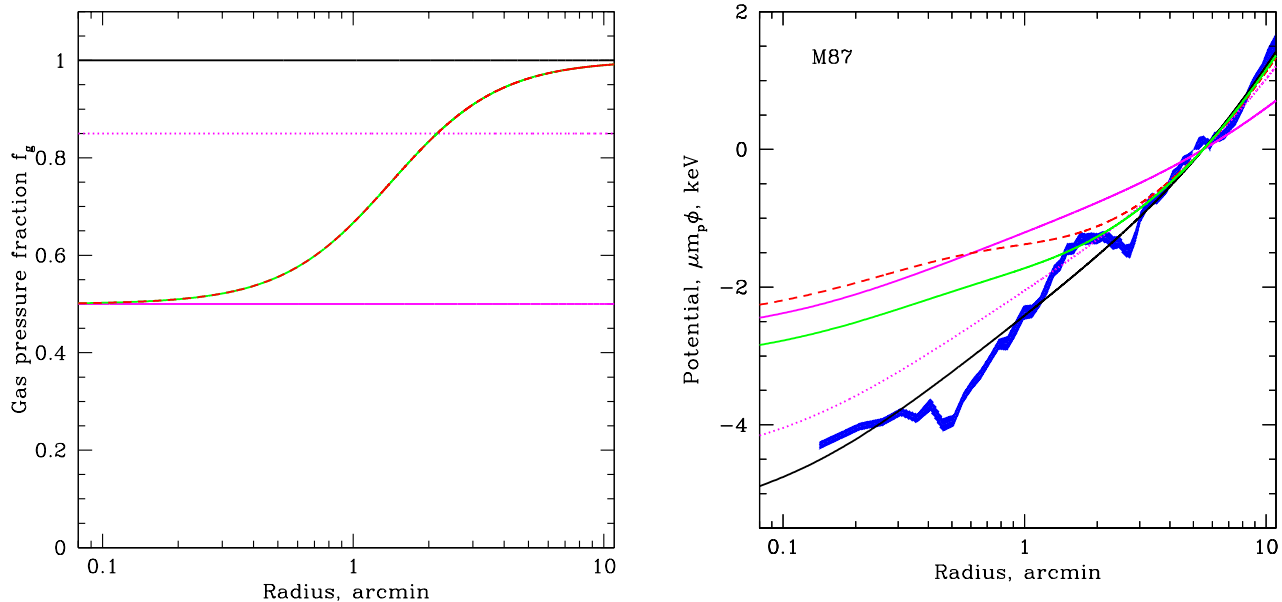


**Figure 10.** **Left:** Various model dependences of the thermal gas fraction  $f_g$  on radius discussed in Section 6. **Right:** Expected potential  $\varphi_X$  that would be derived from X-ray observations for each of the  $f_g$  models shown in the left plot. The color coding is the same in both plots. We assumed that the true potential is the NFW2 model of RK01. Such a potential would be derived from perfect X-ray data if  $f_g = \text{const} = 1$  (thick black solid line). Other  $f_g, \varphi_X$  pairs shown on both plots are: solid magenta line represents  $f_g = \text{const} = 0.5$ ; dotted magenta line represents  $f_g = \text{const} = 0.85$ ; red dashed line represents  $f_g$  given by eq. (12) and  $\varphi_X$  from eq. (11); green solid line represents  $f_g$  given by eq. (12) and  $\varphi_X$  from eq. (13). Note, that the gas pressure fraction curves for the two potentials in green and red (dashed) are identical and they overlap in the left panel. For comparison, the blue curve shows  $\varphi_X$  derived from the Chandra observations of M87 (same curve as shown in Fig. 8). The comparison of black, magenta, red and green lines in the right figure demonstrates the impact of the non-thermal pressure on  $\varphi_X$ . The measured  $\varphi_X$  (blue line) agrees with the optical profile (black line) better than any of the model curves, suggesting that the fraction of nonthermal pressure is on average less than is assumed in any of these models.

rays uniformly mixed with the thermal gas, and cosmic rays contained in bubbles.

### 6.5 Sound waves and shocks

The presence of sound and shock waves formally invalidates our assumption of hydrostatic equilibrium. At any given location the potential derived from X-ray data can be either underestimated or overestimated, depending on the sign of the pressure gradient in the wave. Forman et al. (2005, 2007) identified in the X-ray data a number of quasi-spherical features around M87 which are plausibly caused by shock waves produced by an unsteady outflow of relativistic plasma from the black hole at the center of M87. These shock candidates are located exactly where we see wiggles in the potential (Fig. 10). This is not surprising since, in a spherical shock propagating from the center of the galaxy, the pressure first increases sharply inwards at the front and then decreases in the rarefaction region behind the shock. The potential derived from the X-ray analysis (see eq. 10) will have a ‘dip’ at the position of the shock front and it will then recover from this dip over the rarefaction region. To illustrate such behavior we simulated a spherical shock in the atmosphere of M87 and calculated the potential  $\varphi_X$  which would be derived from X-ray data corresponding to these simulations. Fig. 11 shows the true potential, assumed in the simulations,

with the black line, while the blue line shows  $\varphi_X$  calculated for a Mach 1.2 shock located 2.7’ from the nucleus (see Forman et al. 2007,2008 for details of the shock parameters and the simulations).

For weak shocks/sound waves which are well localized in space (e.g., weak compression waves)  $\varphi_X$  will be affected only in the region where the wave is present, while  $\Delta\varphi_X = \varphi_X(r_2) - \varphi_X(r_1)$  over a range of radii from  $r_1$  to  $r_2$  which covers the entire perturbation will not be affected. Therefore, weak and localized perturbations do not affect the global change of  $\varphi_X$ . In the discussions below that compare  $\varphi_X$  and  $\varphi_{opt}$  (Section 7.1) we focus on radii,  $r_1$  to  $r_2$ , away from the radii most strongly affected by the shock.

### 6.6 Non-luminous gas

In sections 6.1, 6.2 6.3, we have assumed that there is an ‘invisible’ (in X-rays) component contributing to the pressure. As a result, the derived potential  $\varphi_X$  was flatter than the true potential. We can also assume that there is an X-ray ‘invisible’ gas component which contributes to the mass density and has a small filling factor. A cool gas phase with temperature below ‘observable’ X-ray values but coupled to the X-ray emitting phase (e.g., by magnetic fields) would be the simplest example. The  $\varphi_X$  derived from equation (9)

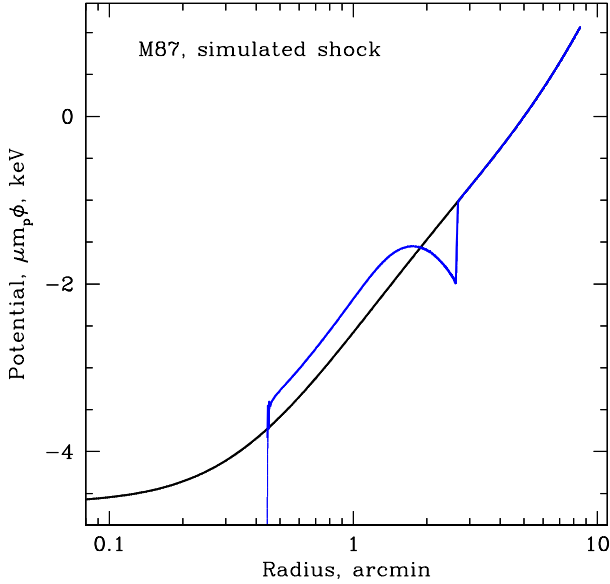


**Figure 11.** Potential ( $\varphi_X$  - blue line) derived using eq. (10) from simulated density and temperature profiles. In these simulations a powerful explosion (with total energy a few  $10^{57}$  erg) at the center of the galaxy drove a shock through the ICM. The data shown in the figure correspond to the time when the shock of Mach number  $\sim 1.2$  is located  $\sim 2'.7$  from the nucleus, the observed radius of the strongest shock in M87. The true potential is shown with the black line. The deviations of  $\varphi_X$  predicted by the shock model from the true underlying potential resemble the deviations between the observed  $\varphi_X$  and  $\varphi_{opt}$  (e.g. blue curve in Fig.10), suggesting that most of the wiggles seen in the observed  $\varphi_X$  are due to the shock.

will be simply:

$$\varphi_X = \int f_m d\varphi, \quad (14)$$

where  $f_m = \rho/\rho_X$  is the ratio of total mass density to the mass density derived from the X-ray analysis. In this case  $f_m > 1$  and the X-ray derived potential will be steeper than the true potential. Although we note this possibility here, for the remainder of the discussion below, we assume that this “non-luminous gas” component does not affect M87 and NGC1399. Otherwise it will be difficult to disentangle the contribution of such a component from that of non-thermal components which affect  $\varphi_X$  in the opposite direction. In the absence of any “non-luminous gas” component, we can place constraints on the non-thermal pressure as we discuss below.

## 7 DISCUSSION

### 7.1 Evaluation of the non-thermal pressure contribution $f_g$

In Fig. 12 the potential derived from X-ray data is plotted against the potential derived from optical data for M87 and NGC 1399 (red shaded areas). If the assumptions used

when deriving the potentials are correct, then one expects to find  $\varphi_X = \varphi_{opt}$  (shown with the dashed lines). If cosmic rays, magnetic fields or micro-turbulence contribute to the pressure in the X-ray emitting gas, then the change of  $\varphi_X$  between two radii will be smaller than the change in  $\varphi_{opt}$ , i.e.  $\Delta\varphi_X = a\Delta\varphi_{opt}$ , where  $a < 1$ . In the simplest case of a constant  $f_g$ , there is a linear relation between the two potentials  $\varphi_X = a\varphi_{opt} + b$ , where  $a = f_g$ . As shown in sections 6.1 and 6.3, if  $f_g$  depends on radius then the relation between the potentials can be more complicated. If  $f_g$  is not constant, but decreases towards small radii, i.e. the role of non-thermal pressure increases towards the center, then  $\varphi_X$  will be even shallower than is prescribed by the relation  $\varphi_X = f_g\varphi_{opt} + b$  (see eq. 11 and 13). Therefore, we can use the relation  $\varphi_X = a\varphi_{opt} + b$ , corresponding to the assumption of constant  $f_g = a$ , to provide a conservative upper limit on the contribution of non-thermal pressure  $1 - f_g$  over the observed range of radii. This upper limit corresponds to an averaged non-thermal pressure contribution over the observed range of radii. The averaging is done with effective “weights” corresponding to the values of the optical potential at each radius. For example, for an isothermal (logarithmic) potential the weight of the radial range from  $r$  up to  $r + \Delta r$  is proportional to  $\ln \frac{r + \Delta r}{r}$ .

A linear fit to the observations of the form  $\varphi_X = a\varphi_{opt} + b$  is shown in Fig. 12 with the thick solid line. For NGC1399,  $a = 0.93$ . For M87  $a = 0.89$  if the WT06 model is used and  $a = 0.975$  for the NFW2 model of RK01. The very closeness of  $a$  to unity in the latter case (NFW2 model) is surely a coincidence given the obvious wiggles in  $\varphi_X(r)$  (Fig. 12). For the two other (less probable) models of RK01 - NFW1 and NFW2 the values of  $a$  are 0.96 and 1.21 respectively. By repeating the fit four times using independent quadrants of the X-ray data (see Section 7.2) we conclude that the statistical uncertainty in these slopes is  $< 0.04$ . Taken at face value, these results mean that the fractional non-thermal contribution to the pressure amounts to 7% for NGC1399 and 2.5-11% (depending on the  $\varphi_{opt}$  model) for M87. These values characterize the non-thermal contribution averaged over the range of radii from  $0'.7$  to  $12'$  in M87 and from  $3''$  to  $5'$  in NGC 1399. Given that systematic uncertainties are present in the data (e.g., due to the shock in M87) it is difficult to provide a precise estimate of the uncertainty associated with this value. If one adopts a more conservative approach of upper limits (rather than measurements) on the non-thermal pressure components, then these limits are  $\sim 10\%$  and  $\sim 20\%$  for NGC 1399 and M87 respectively (see Fig. 12).

Fig. 6 (top panel) shows that, for temperatures characteristic of M87 and NGC1399, fitting multi-phase plasma spectra with a single-temperature model will result in  $\varphi_X$  biased towards shallower values (smaller  $a$ ). Therefore this “multi-phase bias” has the same sign as the non-thermal pressure and can only lead to an overestimation of the non-thermal pressure fraction; thus the upper limits given in the preceding paragraph remain valid. In addition, based on the comparison of spectral fitting in two energy bands (Fig. 5), we do not expect this bias to be strong, at least outside the innermost  $0'.4$  in M87.

Errors in the optical potential profile could also contribute to the observed difference in potentials. In both

galaxies, uncertainties arise from the assumption of spherical symmetry, the restriction to a particular family of parametric halo potentials in the dynamical modeling, and possible systematic errors in deriving the line-of-sight velocity distribution from the observed spectra. These uncertainties are difficult to estimate precisely. Confidence limits within the parametric potentials used for NGC 1399 are given in Fig. 9 and Section 5.2. Thomas et al. (2007) have investigated the uncertainties in the inferred circular velocity curves for a sample of Coma cluster ellipticals which they studied with axisymmetric dynamical models and in a wider range of potentials. In these galaxies, the central mass density is dominated by the luminous matter, independent of the dark matter halo profile used; thus the circular velocities inside  $\simeq 0.5R_e$  are accurately determined, within  $\simeq 5\%$ . At two effective radii, the uncertainties in the inferred circular velocities for their galaxies are  $\simeq 15\%$ . The measurement errors in the observed kinematics for NGC 1399 (Saglia et al. 2000) are smaller than in the Coma ellipticals. However, NGC1399 observations are along only one long slit. Hence, we would expect somewhat smaller uncertainties in NGC 1399. Again the error in the potential is smaller, since the potential is obtained by the integral of the circular velocity curve. However, note that differences  $\phi_{opt} - \phi_{true}$ , in the inferred optical potential profiles are likely to be more slowly varying functions of radius than the variations in  $\phi_X - \phi_{opt}$  seen in Fig. 9.

The  $\phi_X - \phi_{opt}$  difference characterizes the combined contribution of all non-thermal pressure components and the modelling uncertainties of the respective datasets. Under the assumption that modelling uncertainties do not dominate and that the contributions of individual components of the non-thermal pressure all have the same sign, the measured values can be converted to upper limits. For example, fractions of non-thermal pressure support of 10% in M87 and NGC 1399 translate into upper limits on the magnetic field of  $\sim 16$  and  $\sim 10 \mu\text{G}$  respectively (evaluated at a distance from the galaxy center of  $2'$  in M87 and  $1'$  in NGC 1399).

## 7.2 Non-spherical models

We have assumed that the gravitational potential in both M87 and NGC 1399 is spherical. The ellipticity of the optical isophotes of M87 is near zero at the center, rising to 0.4 at  $10'$ , while the ellipticity of the X-ray isophotes outside  $5'$  is 0.1–0.15, with the same position angle (Böhringer et al. 1997) (see Fig.1). The ellipticity of the optical isophotes of NGC 1399 is about 0.1 out to  $10'$  (Dirsch et al. 2003). The X-ray image of NGC1399 looks more disturbed (see Fig. 2) than the optical image and has an ellipticity of 0.34 at the effective radius of the galaxy (Diehl & Statler 2007). The shapes of the X-ray emitting gas and the stellar distribution need not be the same in the common potential, since the velocity-dispersion tensor of the stars is not necessarily isotropic.

Thus both galaxies exhibit a modest level of non-axisymmetry in their X-ray and optical isophotes. We can assess the impact of these asymmetries on the X-ray derived potential by using the data in individual (independent) wedges and deriving the corresponding X-ray potentials as shown in Fig. 13. Within each  $90^\circ$  wedge, centered at the optical center of the galaxy, we assume that

the gas properties depend only on the distance from the center and we repeat our previous analysis up to fitting the  $\varphi_X = a\varphi_{opt} + b$  relation. The innermost and outermost bins, which have large statistical uncertainties, were excluded from the fit (as shown by thin vertical lines in Fig. 13). The values  $a_{M87,NWF2} = \{1.04, 0.98, 1.03, 0.95\}$  and  $a_{NGC1399} = \{0.95, 0.93, 0.92, 0.95\}$  were found for the NW, NE, SE and SW wedges in the two galaxies. If WT06 model is used for M87 then  $a_{M87,WT06} = \{0.93, 0.86, 0.89, 0.87\}$ . The root-mean-square deviations of  $a$  from the mean values are 3-4% for M87 (depending on the optical profile used) and 1.5% for NGC1399. These modest deviations characterize the total uncertainty associated with the apparent non-axisymmetry in the X-ray isophotes of these two galaxies. Note that the observed scatter in slope between the four quadrants also represents an upper limit to the statistical uncertainties in the slope, although for these datasets we believe that the scatter is mostly due to non-axisymmetry rather than statistics.

An additional uncertainty, probably of a few per cent, is related to the freedom of choosing the range of radii used for fitting the  $\varphi_X = a\varphi_{opt} + b$  relation. This is more serious for M87 where the presence of a shock clearly makes the results more sensitive to the choice of the radial bins.

Another concern is that the actual deviations from spherical symmetry may be larger than the observations indicate, if the galaxy is an approximately axisymmetric system that is viewed pole-on. The effects of a non-spherical potential on X-ray estimates of mass or potential have been modelled by Piffaretti, Jetzer & Schindler (2003) for an ellipsoidal  $\beta$ -model (see also Gavazzi 2005 for the analysis of axisymmetric NFW profiles). Although Piffaretti et al. were concerned with clusters of galaxies, their results apply to galaxies as well. They found that if (i) the galaxy potential is axisymmetric and viewed pole-on and (ii) its mass is estimated from the temperature and distribution of hot gas with the assumption that the potential is spherical; then, the derived mass within a spherical radius is typically in error by only a few per cent, if the axis ratio of the potential is varied within plausible limits (typically  $\pm 40\%$ ). We note that for the model considered by Piffaretti et al. (2003) (ellipsoidal  $\beta$ -model distribution of isothermal gas) in the limiting case of the radius much larger than the  $\beta$ -model core radii the deprojected potential/mass profiles are exact for any orientation of the galaxy/cluster with respect to the line of sight (see Appendix B). While the above assumptions (e.g. isothermality) are not in general met, this result suggests that the effect of triaxiality can be small. We provide a more quantitative analysis of the triaxiality on real systems in future work.

The effects of a non-spherical potential on optical estimates of mass are more difficult to model. The simplest approach is based on the tensor virial theorem (e.g., Binney & Tremaine 2008). If (i) an axisymmetric one-component self-gravitating stellar system is viewed pole-on; (ii) the density of stars in the system is constant on spheroids of eccentricity  $e$ ; and (iii) the mass of the system is estimated using the virial theorem for spherical systems; then the derived mass will exceed the actual mass by a factor  $f$ , where

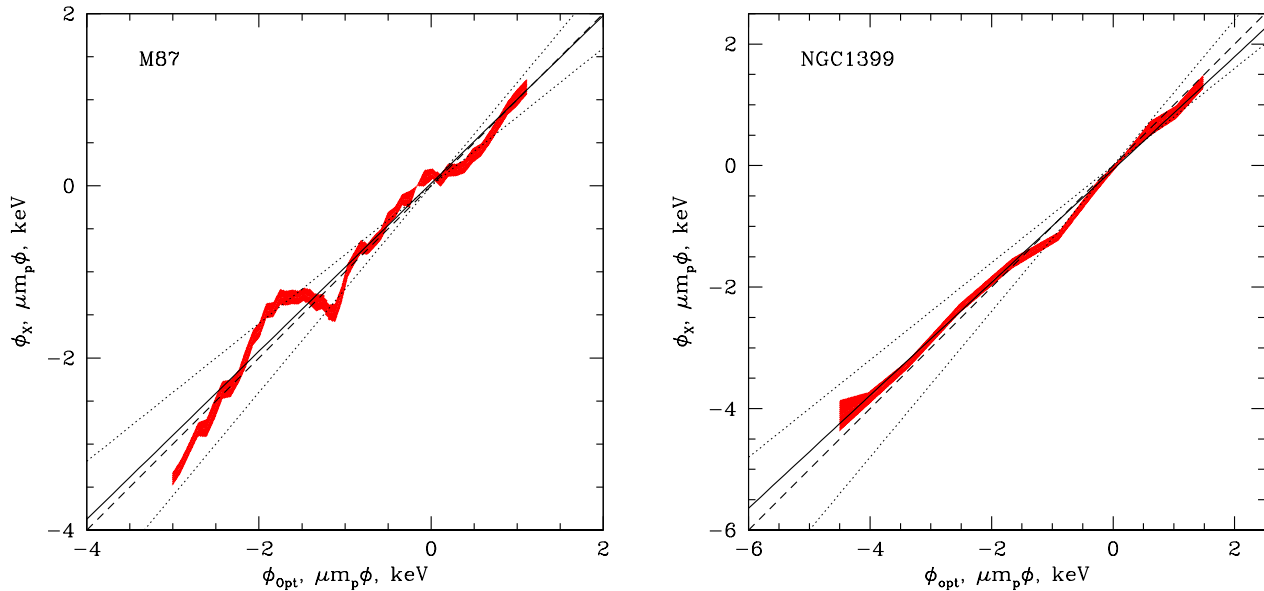


**Figure 12.** Potential derived from X-ray data plotted versus the potential derived from optical data for M87 and NGC 1399 (red shaded areas). The thick solid line is a formal linear fit  $\varphi_X = a\varphi_{opt} + b$ . In M87 the value of  $a$  is 0.975 for NWF2 model of RK01 and 0.89 for WT06 model. In NGC 1399  $a = 0.93$  for Kronawitter et al. 2000 model. The thick dashed line shows the dependence  $\varphi_X = \varphi_{opt}$ , while thin dotted lines correspond to  $a=0.8$  and  $1.2$ . For both objects, values of  $a$  close to unity imply that the fraction of non-thermal pressure is  $\lesssim 0.1$ .

$$f(e) = \begin{cases} 3 \frac{1-e^2}{e^2} \left( \frac{1}{\sqrt{1-e^2}} - \frac{\sin^{-1} e}{e} \right) & \text{oblate systems} \\ 3 \frac{\sqrt{1-e^2}}{e^2} \left( \frac{1}{2e} \log \frac{1+e}{1-e} - 1 \right) & \text{prolate systems,} \end{cases} \quad (15)$$

where  $e = \sqrt{1 - b^2/a^2}$  and  $b/a$  is the axis ratio. For a plausible range of axis ratio, say  $0.5 < b/a < 1$ ,  $f$  varies only between 0.79 (most oblate) and 1.04 (most prolate), suggesting that the error in the optical potential due to asphericity is likely to be small.

It should also be stressed that the probability that either of the studied galaxies is strongly oblate or prolate and viewed pole-on is rather low. The distribution of ellipticities in a sample of brightest cluster ellipticals similar to M87 and NGC1399 was studied by Porter et al. (1991). They modelled the distribution of axis ratios  $q$  as a Gaussian with mean  $\mu$  and dispersion  $\sigma_e$ , and found  $\mu = 0.66$ ,  $\sigma_e = 0.09$  if the galaxies were assumed to be oblate, and  $\mu = 0.69$ ,  $\sigma_e = 0.09$  if the galaxies were prolate (at a radius of 15 kpc, corresponding to  $3'.2$  in M87 and  $2'.6$  in NGC 1399). The apparent axis ratios in M87 and NGC1399 at this radius are 0.2 and 0.1 respectively. The conditional probability distribution of the intrinsic axis ratio, given the apparent axis ratio, can be computed from these data. The probability that the intrinsic axis ratio in the stellar light distribution is as small as 0.5 is only 2% if the galaxies are oblate and 6% if they are prolate. The potential due to the stars is, of course, more nearly spherical than the distribution of the stars themselves.

Finally, we point out that substantial errors due to asphericity are likely to affect the optical and X-ray estimates

of the potential in different ways. The close agreement between the X-ray and optical potentials, seen in Figs. 8 and 9, would be an unlikely coincidence if any asphericity were significantly affecting the derived potentials.

### 7.3 Is the small non-thermal component consistent with AGN-heated cluster cool cores?

The central region of M87 is a classic example of a cooling flow – a region where gas radiative losses are high and an external source of energy is required if one wants to have a quasi-steady state without large net cooling of the gas, as indicated by the recent XMM-Newton RGS data (e.g., Peterson et al. 2003). A plausible source of energy for gas reheating is the activity of the central black hole, mediated by the outflow of relativistic plasma. Actual gas heating might be due to dissipation at shock fronts (e.g., David et al. 2001) or in sound waves (if the medium is viscous, has appreciable thermal conductivity or is strongly non-uniform, e.g., Fabian 2003, 2005; Ruszkowski et al. 2004a, 2004b; Heinz & Churazov 2005) or through an intermediate step of generating gas turbulence, which eventually dissipates its energy (e.g., Churazov et al. 2001, 2002). We now test whether our results on the non-thermal forms of pressure are consistent with this picture.

First, we directly see bubbles of relativistic plasma (as radio bright regions and as ‘cavities’ in X-rays). If the M87 gas is in a quasi-equilibrium state with cooling losses, on average compensated by heating, then the mechanical power of the outflow should be related to the gas cooling losses. As ar-

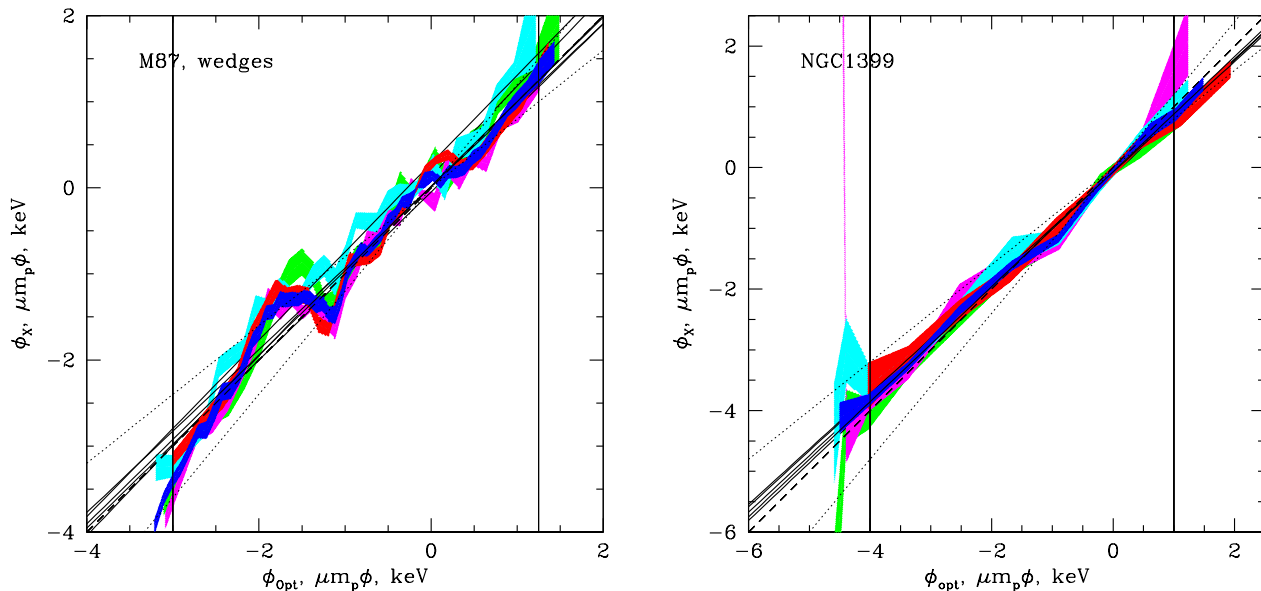


**Figure 13.** Potentials derived from X-ray data for M87 (left) and NGC1399 (right) in four  $90^\circ$  wedges (green, magenta, cyan and red for NW, NE, SE and SW wedges respectively), plotted against the optically derived potentials (RK01 for M87 and Kronawitter et al. 2000 for NGC1399). The centers of the wedges coincide with the optical centers of the galaxies. The blue curves in each plot show the X-ray potentials derived from the full  $0\text{--}360^\circ$  data. Black solid lines show the linear least-square fits  $\varphi_X = a\varphi_{opt} + b$  for each wedge and for the complete dataset. The innermost and outermost bins, which have large statistical uncertainties, were excluded from the fit (thin vertical lines). As in Fig. 12, the thick dashed line shows the dependence  $\varphi_X = \varphi_{opt}$ , i.e.  $a = 1$ , while the thin dotted lines correspond to  $a=0.8$  and  $1.2$ . Clearly the slopes  $a$  derived for individual independent wedges agree well with each other, with root-mean-square deviations of 4.5% for M87 and 1.5% for NGC1399. The deviations characterize the overall uncertainties in  $a$  that are caused by the apparent asymmetries in the X-ray images and by statistical errors.

gued in Churazov et al. (2001), Begelman (2001), and Nulsen et al. (2006), the efficiency of energy transfer from a relativistic outflow to the gas is high, when the outflow subsonically crosses regions with large pressure gradients. In this case, one can simply assume that the power of the outflow is equal to the cooling losses. The total energy of the relativistic plasma bubbles in the region can then be estimated from the balance of powers as  $\mathcal{E}/t_{cross} \sim \mathcal{E}_{thermal}/t_{cool}$ , where  $\mathcal{E}_{thermal}$  is the gas thermal energy,  $t_{cool}$  is the gas cooling time and  $t_{cross}$  is the time each bubble spends inside the region where it deposits a significant fraction of its enthalpy. For example, consider a 10 kpc region around M87. For an electron density  $n_e = 2 \times 10^{-2} \text{ cm}^{-3}$  and a temperature  $T_e = 1.7 \text{ keV}$ , the cooling time  $t_{cool} \sim 7 \times 10^8 \text{ yr}$ . On the other hand, the rise velocity of large buoyantly driven bubbles is  $\zeta c_s$  where  $c_s$  is the sound speed and  $\zeta$  is a factor of order 0.5 (e.g., Churazov et al. 2001). Thus,  $t_{cross} \approx 3 \times 10^7 \text{ yr}$  for the 10 kpc region. Therefore, bubbles of relativistic plasma should, on average, account for a fraction  $t_{cross}/t_{cool} \sim 0.05$  of the total energy (or volume). This is consistent within a factor of 2 with the results we obtained from Fig. 12. Note that since the electron density in a typical cooling flow (e.g., in M87) scales approximately as  $n_e \propto r^{-1}$ , then  $t_{cool} \propto 1/n_e \propto r$  and  $t_{cross} \propto r$ . Therefore the above estimate of  $t_{cross}/t_{cool}$  is only weakly sensitive to the radius used to evaluate all quantities.

We can now check whether our limits exclude turbu-

lence as an intermediate reservoir of energy in the process: moving bubbles  $\rightarrow$  turbulence  $\rightarrow$  viscous dissipation and gas heating as suggested by Chandran (2004) and Rebusco et al. (2005, 2006). In this case, the energy dissipation rate of the turbulent motions should be approximately equal to the gas cooling losses:

$$C \mu m_p n \frac{v_{turb}^3}{l_{turb}} \approx \frac{3}{2} n k T, \quad (16)$$

where  $v_{turb}$  and  $l_{turb}$  are the characteristic velocity and spatial scale of energy containing eddies,  $n$  is the gas particle density and  $C$  is a dimensionless constant of the order of unity. According to a recent compilation by Dennis & Chandran (2005),  $C \simeq 0.42$ . If the energy in the micro-turbulence is constrained to be less than a fraction  $\xi$  of the thermal energy, then

$$\frac{1}{2} \mu m_p n v_{turb}^2 \lesssim \xi \frac{3}{2} n k T, \quad (17)$$

and then

$$\frac{v_{turb}}{l_{turb}} \gtrsim \frac{1}{2C} \frac{1}{\xi} \frac{1}{t_{cool}}. \quad (18)$$

Therefore  $v_{turb} \gtrsim 20 \left( \frac{l_{turb}}{1 \text{ kpc}} \right) \left( \frac{\xi}{0.15} \right)^{-1} \text{ km s}^{-1}$ . This condition is likely satisfied in the gas around M87 (if it is indeed turbulent), since the characteristic size of individual bubbles

is of order 1–3 kpc and their velocities are expected to be significantly higher, a few  $10^2$  km s $^{-1}$  (Churazov et al. 2001).

#### 7.4 The history of the ICM enrichment with cosmic rays

Our constraints on the non-thermal pressure are consistent with the current paradigm of re-heating of gas in “cooling flows”, which assumes a balance between radiative cooling and mechanical heating of the gas. On the other hand, our conclusion that the fraction of the energy density in the form of cosmic rays and magnetic fields is  $\lesssim 10\text{--}20\%$  provides an important constraint on the history of the ICM. In particular, these limits apply to the mixing of thermal plasma with relativistic plasmas, as well as the generation of cosmic rays by shocks in the bulk of the ICM. Generally, it is believed that the energy density of cosmic rays is dominated by protons rather than electrons and the particles with the lowest  $\gamma$  provide the most important contribution to the energy density. The lifetime of a transrelativistic proton (Lorentz factor of 2) with respect to Coulomb energy losses in a cluster plasma with electron density of  $10^{-2}$  cm $^{-3}$  is roughly 5 Gyr. Therefore, the energy density of relativistic protons is largely conserved, except for adiabatic losses, during the lifetime of the cluster (transrelativistic electrons have of course much shorter lifetimes). This implies that our constraints on the energy density of cosmic rays in the cores of M87 and NGC 1399 today actually limit the presence of relativistic protons during the entire history of the same gas lump, provided that relativistic particles are not able to diffuse out of the lump. The constraints on cosmic ray energy density in the past may be even tighter, if cosmic rays were originally deposited into a gas lump which had much higher entropy than is observed today and has lost the excess entropy by cooling. Indeed, if relativistic protons experience only adiabatic losses, then their energy density changes with gas density as:

$$\varepsilon'_{cr} = \varepsilon_{cr} \left( \frac{\rho'_{gas}}{\rho_{gas}} \right)^{\gamma_{cr}}, \quad (19)$$

where  $\rho_{gas}$  and  $\varepsilon_{cr}$  denote the thermal gas density and the energy density of cosmic rays observed now;  $\gamma_{cr} = 4/3$  is the adiabatic index of cosmic rays. All quantities measured at a different time are denoted with a prime. The thermal energy is by definition

$$\varepsilon'_{gas} = \varepsilon_{gas} \left( \frac{\rho'_{gas} T'_{gas}}{\rho_{gas} T_{gas}} \right). \quad (20)$$

Thus

$$\frac{\varepsilon'_{cr}}{\varepsilon'_{gas}} = \frac{\varepsilon_{cr}}{\varepsilon_{gas}} \times \left( \frac{\rho'_{gas}}{\rho_{gas}} \right)^{\gamma_{cr}-1} \frac{T_{gas}}{T'_{gas}}. \quad (21)$$

Therefore, a constraint on the energy density of cosmic rays now  $\varepsilon_{cr}/\varepsilon_{gas} \lesssim 0.1$ , for M87 and NGC 1399, can be transformed into constraints on  $\varepsilon'_{cr}/\varepsilon'_{gas}$  in the same gas lump. This is illustrated in Fig. 14. Solid and open squares show the gas density and temperature observed in the cores of M87 and NGC 1399 today. Along the solid lines ( $T \propto \rho^{\gamma_{cr}-1}$ ), the ratio  $\varepsilon'_{cr}/\varepsilon'_{gas}$  is constant. Therefore, if, in the past, the gas lump we see now in the core of M87 or NGC 1399 had a density and a temperature along the thick solid line, then the constraint on the energy density of cosmic rays would be the

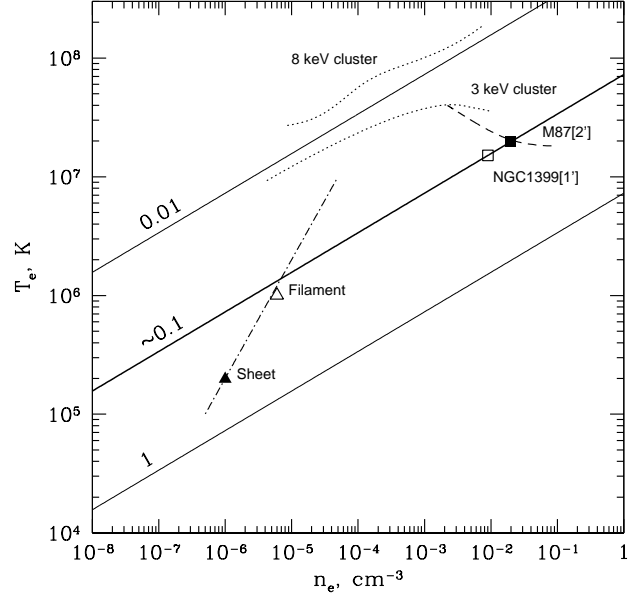


**Figure 14.** Constraints on the energy density of cosmic rays during the evolution of gas lumps presently seen in the cores of M87 and NGC 1399. The ratio  $\varepsilon'_{cr}/\varepsilon'_{gas}$  is constant along the solid lines. If the gas had in the past a density and temperature along the thick solid line, then at that time the constraint on energy density of cosmic rays is the same as now:  $\varepsilon'_{cr}/\varepsilon'_{gas} \lesssim 0.1$ . Thin solid lines show the parameters for which present day constraints transform into  $\varepsilon'_{cr}/\varepsilon'_{gas}$  limits of 0.01 and 1, respectively. For comparison we show a few typical states of the IGM/ICM, ranging from warm gas in sheets and filaments (triangle symbols and the dash-dotted line) in the large scale structure to shock-heated gas (3 and 8 keV) in galaxy clusters (dotted curves). The dashed line shows the locus of  $(n_e, T_e)$  points taken from radially averaged profiles of the ICM in M87 at distances from 0'.5 to 5' from the galaxy center.

same as now:  $\varepsilon'_{cr}/\varepsilon'_{gas} \lesssim 0.1$ . The two thin solid lines show the parameters for which present day constraints transform into  $\varepsilon'_{cr}/\varepsilon'_{gas}$  limits of 0.01 and 1 respectively. For comparison, we show a few typical states of the IGM/ICM, ranging from warm gas in sheets and filaments (triangle symbols and the dash-dotted line) in the Large Scale Structure to shock heated gas (3 and 8 keV) in galaxy clusters (dotted curves). The cluster data are taken from simulations of Nagai, Vikhlinin & Kravtsov (2007) for  $z = 0$ . The data for 3 keV and 8 keV clusters were used and the radial profiles plotted in Fig. 14 correspond to distances from  $\sim 70$  kpc to  $\sim 2$  Mpc from the cluster center. The main conclusion of this simple exercise is that if the gas in the core of M87 or NGC 1399 were in the past shock heated above the upper solid line, the energy density of cosmic rays in the gas, at that time, was less than 1–2% of the thermal energy density. We emphasize again that this conclusion is based on the assumption that cosmic rays dominating the energy density (presumably low energy protons) are not able to diffuse out of the gas lump and they suffer only adiabatic losses. Allowing diffusion would essentially imply that our upper limits are applicable only to the moment of observation.



Gamma-ray observations of clusters (Reimer et al. 2003) do limit the presence of cosmic rays, in particular protons, to less than  $\sim 20\%$  of the gas thermal energy (e.g., Pfrommer & Ensslin 2004). It is interesting that Brunetti et al. (2007) have recently derived an upper limit on the contribution of relativistic protons to the gas pressure based on radio upper limits for clusters without radio halos. While the actual limit on protons is sensitive to the assumed strength of the magnetic field, for many clusters the upper limit falls below 1% (for  $> \mu G$  fields) of the thermal pressure measured from the X-ray gas.

## 7.5 Clusters of galaxies

X-rays can be used to constrain mass/potential profiles of elliptical galaxies as long as the galaxy is gas rich and the contribution of individual stellar-mass systems to the X-ray emission (e.g., Revnivtsev et al. 2007) can be neglected. This implies that the X-ray analysis described in this paper can be applied to massive ( $\gtrsim 10^{11} M_{\odot}$ ) systems. The most massive ellipticals often dwell at the centers of groups/clusters (galaxies like NGC1399 and M87). For these systems, X-ray observations can be used over a broad range of radii, from a fraction of the central galaxy effective radius to distances almost comparable to the cluster virial radius. The optical data on stellar kinematics are mostly useful up to 1-2  $R_e$ . This range of radii can be extended to a few  $R_e$  with tracers such as globular clusters and planetary nebula (e.g., Samurovic & Danziger 2006, Wu & Tremaine 2006, Douglas et al., 2007), and to much larger radii using satellite galaxies or weak gravitational lensing. The comparison of lensing and X-ray masses made by Mahdavi et al. (2007) for a sample of 18 clusters yielded  $M_X/M_L = 1.03 \pm 0.07$  and  $M_X/M_L = 0.78 \pm 0.09$  at radii corresponding to overdensities of 2500 and 500 respectively. These results, which characterize cluster properties at radii  $\sim 0.3$ -1.5 Mpc, are broadly consistent with our findings for the inner few tens of kpc. When combined with our work, these results suggest that the contribution of non-thermal components to pressure does not exceed  $\sim 10$ -20% over the entire cluster volume, as long as the system has not recently experienced a major merger. In numerical simulations of structure formation there is a substantial (in the range from a few per cent to tens of percent) contribution from residual stochastic gas motions to the pressure (e.g., Evrard 1990; Nagai, Vikhlinin & Kravtsov 2007), especially in the outer regions of clusters. If one accounts for this apparently unavoidable contribution, the remaining room for cosmic rays and magnetic fields shrinks further, to  $\leq 10\%$  over the whole cluster volume. Note however that the conditions in the cluster outskirts and core are markedly different and it is unlikely that a universally applicable limit can be easily derived.

## 8 CONCLUSIONS

Using Chandra observations of M87 and NGC 1399 we derive the gravitational potential profiles of these two galaxies and compare them with the potentials derived from optical data. Both the X-ray and optical methods – one based on the hydrostatic equilibrium of hot gas and the other on stellar dynamics – give consistent changes of the potential

to within  $\sim 10$ -20% over a broad range in radial distance. In M87, several obvious wiggles in the X-ray derived profile can plausibly be attributed to a spherical shock propagating through the ICM.

These results suggest that the combined contribution of cosmic rays, magnetic fields and micro-turbulence  $\lesssim 10$ -20% of the gas thermal energy. These findings are consistent with the current paradigm of cool cluster cores, based on the assumption that AGN activity regulates the thermal state of the gas by injecting energy into the ICM.

We also show that the limit of  $\sim 10$ -20% on the energy density in the form of relativistic protons applies not only to the current state of the gas, but essentially to the entire history of the ICM, provided that cosmic ray protons evolve adiabatically and their spatial diffusion is suppressed.

The comparison of  $\varphi_X$  and  $\varphi_{opt}$  is presented here for two objects only. Given the uncertainties in optical and X-ray modelling and peculiarities of the considered objects (e.g. notable shock in M87) it is desirable to extend the analysis to a larger sample. This project is under way and the results will be reported in subsequent publications.

## 9 ACKNOWLEDGEMENTS

We are grateful to the referee for important comments and suggestions. This work was supported by the DFG grant CH389/3-2, NASA contracts NAS8-38248, NAS8-01130, NAS8-03060, the program “Extended objects in the Universe” of the Division of Physical Sciences of the RAS, the Chandra Science Center, the Smithsonian Institution, MPI für Astrophysik, and MPI für Extraterrestrische Physik. ST acknowledges support from a Humboldt Research Award.

## APPENDIX A: A NOTE ON DEPROJECTION TECHNIQUES

Mathematically the deprojection procedure described in Section 4 is identical (except for the  $1/\eta$  factor) to the conventional onion-peeling algorithm (e.g., Fabian et al. 1980) if the number of spherical shells is equal to the number of radial annuli and a unique and exact solution exists. However our formulation (i.e. eq. 3) works also for different numbers of shells/annuli. Typically  $n_s < n_a$ , so the inversion problem is overdetermined, but problems with  $n_s > n_a$  are also easily tractable with the additional condition that the solution should have a minimal norm. Our method also provides an explicit expression for the statistical uncertainties in the solution.

Compared to XSPEC’s `project` our deprojection method is much faster, given the large number of radial shells used here, since it avoids simultaneous fitting of many parameters. The expectation values are the same for our method, the onion-peel algorithm and XSPEC’s `project` if the spectral model is the correct one and the assumption of spherical symmetry holds. If, however, one of the above assumptions is incorrect, none of the approaches yields a correct result. The `project` results can be made more physical by imposing constraints on the parameters (e.g., non-negative fluxes in every spherical shell), but at the expense of solving

a much more difficult problem of finding the true minimum in a multi-dimensional space.

One particular application of XSPEC's the onion peeling `project` that is sometimes used is fitting one spherical shell at a time and moving from outside in. This is faster since only one spectrum is fitted at each step. This procedure requires the spectral model to be specified in each outer shell to be able to fit the inner shells, since the contribution of these shells to the inner shells is evaluated using the spectral model (convolved with the instrument effective area and resolution). In contrast in our approach the observed  $1/\eta$  spectra are "subtracted" from the inner shells (after appropriate scaling to account for geometry of shells) and the spectral analysis deferred to the final step of fitting deprojected spectra. Hence, any incorrect model assumptions are not propagated into all the interior shells. Therefore, our deprojection analysis requires only assumptions about the geometry of the cluster.

The bottom line is that all techniques should yield consistent results if underlying assumptions (e.g. spherical symmetry and spectral model) are correct. Our deprojection procedure is especially simple and efficient if many radial bins (spherical shells) are used.

## APPENDIX B: X-RAY MASS AND POTENTIAL OF A NON-SPHERICAL CLUSTER.

Here we prove the following result, mentioned in Section 7.2: Consider gas that is in hydrostatic equilibrium in a non-spherical gravitational potential. Assume that (i) the gas density is characterized by a power law in radius (a large radius limit of the ellipsoidal  $\beta$ -model), that is,

$$\rho_{gas}(r, \theta, \phi) = f(\theta, \phi) r^{-\gamma}, \quad (\text{B1})$$

where  $(r, \theta, \phi)$  are the usual spherical coordinates and  $f(\theta, \phi)$  is an arbitrary positive function; and (ii) the gas is isothermal. Then the gravitational mass within a sphere of given radius and the difference in gravitational potential between any two radii at the same  $(\theta, \phi)$  are given correctly by an analysis that assumes that the gravitational potential and the gas density are spherically symmetric.

To prove this, we write the hydrostatic equilibrium equation for an isothermal gas,

$$\rho_{gas}(r, \theta, \phi) \propto \exp[-\mu m_p \varphi(\mathbf{r})/kT]. \quad (\text{B2})$$

Equating this to (B1) and taking the log, we have

$$\varphi(r, \theta, \phi) = \frac{kT}{\mu m_p} [\gamma \log r - \log f(\theta, \phi)]. \quad (\text{B3})$$

The corresponding density distribution is

$$\begin{aligned} \rho(r, \theta, \phi) &= \frac{1}{4\pi G} \nabla^2 \varphi(r, \theta, \phi) \\ &= \frac{kT}{4\pi G \mu m_p} \left[ \frac{\gamma}{r^2} - \nabla^2 \ln f(\theta, \phi) \right]. \end{aligned} \quad (\text{B4})$$

Here we implicitly assume that  $f(\theta, \phi)$  corresponds to a physically sound density distribution, i.e.,  $\rho(r, \theta, \phi) \geq 0$  in eq. (B4). For this distribution the gravitating mass within a sphere with radius  $r$  is:

$$M(R) = \int_{|\mathbf{r}| < R} d\mathbf{r} \rho(r, \theta, \phi)$$

$$\begin{aligned} &= \frac{kT}{\mu m_p G} \left[ \gamma r - \int_{|\mathbf{r}| < R} d\mathbf{r} \nabla^2 \ln f(\theta, \phi) \right] \\ &= \frac{\gamma kT}{\mu m_p G} r, \end{aligned} \quad (\text{B5})$$

since from the divergence theorem  $\int_{|\mathbf{r}| < R} d\mathbf{r} \nabla^2 \ln f(\theta, \phi) = \oint_{|\mathbf{r}|=R} \nabla \ln f(\theta, \phi) \cdot d\mathbf{s} = 0$ , where the second integration is done over a surface of a sphere with radius  $R$ .

If we assume spherical symmetry when analyzing this cluster (with arbitrary orientation of the main axis relative to the line of sight), we will of course recover the same power law dependence of the density,  $\rho_X \propto r^{-\gamma}$ . Then the change in the potential derived from X-ray data will be:

$$\begin{aligned} \Delta \varphi_X &= \varphi_X(r_2) - \varphi_X(r_1) \\ &= \frac{kT}{\mu m_p} \ln \rho_X(r_1)/\rho_X(r_2) = \frac{\gamma kT}{\mu m_p} \ln(r_2/r_1). \end{aligned} \quad (\text{B6})$$

This is exactly the change of the true potential along any direction (eq. B3).

The derived mass within radius  $r$  will be:

$$M_X(r) = -\frac{r^2}{G} \frac{1}{\rho_X} \frac{dP_X}{dr} = \frac{r^2}{G} \frac{1}{r} \frac{kT}{\mu m_p} \frac{d \log \rho_X}{dr} = \frac{\gamma kT}{\mu m_p G} r, \quad (\text{B7})$$

where  $P_X = kT\rho_X/\mu m_p$ . This is the correct value of the mass within the sphere of radius  $r$  (eq. B5). Thus, if the above conditions are met (isothermal gas with a power law density dependence), the X-ray analysis yields the correct spherically averaged mass and potential difference along any radius vector, independent of the orientation of the triaxial potential with respect to the line of sight. In other words - treating the triaxial system as spherically symmetric and performing a deprojection analysis as for a perfectly spherically symmetric cluster yields the correct answer on the potential/mass. The same is true for the X-ray analysis applied to any wedge, no matter how narrow it is.

## REFERENCES

- Arnaud K. A., 1996, ASPC, 101, 17  
 Begelman M. C., 2001, ASPC, 240, 363  
 Belsole E. et al. 2001, A&A, 365, L188  
 Binney J., Mamon G., MNRAS, 200, 361  
 Binney J., Tremaine S., 2008, Galactic Dynamics (2nd ed.), Princeton Univ. Press, Princeton, NJ  
 Böhringer H., Voges W., Fabian A. C., Edge A. C., Neumann D. M., 1993, MNRAS, 264, L25  
 Böhringer H. et al., 2001, A&A, 365, L181  
 Böhringer H. Neumann, D. M., Schindler, S., Huchra, J. P., 1997, ApJ, 485, 439  
 Brunetti G., Venturi T., Dallacasa D., Cassano R., Dolag K., Giacintucci S., Setti G., 2007, ApJ, 670, L5  
 Buote D. A., Tsai J. C., 1995, ApJ, 439, 29  
 Buote D. A., 2000, ApJ, 539, 172  
 Buote D. A., 2002, ApJ, 574, L135  
 Chandran B.D.G., 2004, ApJ, 616, 169  
 Pellegrini S., Ciotti L., 2006, MNRAS, 370, 1797  
 Churazov E., Gilfanov M., Forman W., Jones C., 1996, ApJ, 471, 673  
 Churazov E., Brüggén M., Kaiser C. R., Böhringer H., Forman W., 2001, ApJ, 554, 261

- Churazov E., Sunyaev R., Forman W., Böhringer H., 2002, MNRAS, 332, 729
- Churazov E., Forman W., Jones C., Böhringer H., 2003, ApJ, 590, 225
- David L. P., Nulsen P. E. J., McNamara B. R., Forman W., Jones C., Ponman T., Robertson B., Wise M., 2001, ApJ, 557, 546
- David, L., Jones, C., Forman, W., Vargas, I. and Nulsen, P., 2006, ApJ, 653, 207
- Dickey J. M., Lockman F. J., 1990, ARA&A, 28, 215
- Diehl S., Statler T. S., 2007, ApJ, 668, 150
- Dirsch B., Richler T., Geisler D., Forte J. C., Bassino L. P., Gieren, W. P., 2003, AJ, 125, 1908
- Dennis T. J., Chandran B. D. G., 2005, ApJ, 622, 205
- Douglas N.G., et al., 2007, ApJ, 664, 257
- Evrard A. E., 1990, ApJ, 363, 349
- Fabian A. C., Willingale R., Pye J. P., Murray S. S., Fabiano G., 1980, MNRAS, 193, 175
- Fabian A., Sanders J., Allen S., Crawford C., Iwasawa K., Johnstone R., Schmidt R., Taylor G. 2003, MNRAS, 344, L43
- Fabian A., Reynolds C., Taylor G., Dunn R. 2005, MNRAS, 363, 891
- Forman, W., Jones, C., Tucker, W., 1985, ApJ, 293, 102
- Forman W. et al., 2005, ApJ, 635, 894
- Forman W. et al., 2007, ApJ, 665, 1057
- Forman W. et al., 2008, ApJ, to be submitted
- Fukazawa Y., Botoya-Nonesca J. G., Pu J., Ohto A., Kawano N., 2006, ApJ, 636, 698
- Gavazzi R., 2005, A&A, 443, 793
- Gerhard, O., MNRAS, 1993, 265, 213
- Graham, A., Colless, M., Busarello, G., 1998, in Zaritsky, D., ed., Galactic Halos: A UC Santa Cruz Workshop. Astronomical Society of the Pacific Conference Proceedings 136, 257
- Heinz, S., Churazov, E., 2005, ApJL, 634, L141
- Hickox R. C., Markevitch M., 2006, ApJ, 645, 95
- Humphrey, P., Buote, D., Gastaldello, F., Zappacosta, L., Bullock, J., Brighenti, F., Mathews, W., 2006, ApJ, 646, 899
- Kronawitter A., Saglia R. P., Gerhard O., Bender R., 2000, A&AS, 144, 53
- Lokas E. L., Mamon G. A., 2003, MNRAS, 343, 401
- Mahdavi A., Hoekstra H., Babul A., Henry J. P., 2007, arXiv:0710.4132
- Markevitch M. et al., 2000, ApJ, 541, 542
- Markevitch, M. 2001, Chandra calibration memo, <http://asc.harvard.edu/cal/>, “ACIS,” and “ACIS Background” and <http://xc.harvard.edu/contrib/maxim/acisbg/COOKBOOK>
- Markevitch M., Vikhlinin A., 2007, PhR, 443, 1
- Matsushita K., Belsole E., Finoguenov A., Böhringer H., 2002, A&A, 386, 77
- Mathews, W. 1978, ApJ, 219, 413
- McLaughlin D. E., 1999, AJ, 117, 2398
- Merritt, D., 1993, ApJ, 413, 97
- Nagai D., Vikhlinin A., Kravtsov A. V., 2007, ApJ, 655, 98
- Navarro J. F., Frenk C. S., White S. D. M., 1996, ApJ, 462, 563
- Nulsen, P. E. J., Jones, C., Forman, W., David, L., McNamara, B., Rafferty, D., Birzan, L., Wise, M., 2006, in Böhringer H., Schuecker P., Pratt G. W., Finoguenov A., eds, Heating vs. Cooling in Galaxies and Clusters of Galaxies. Springer-Verlag, Berlin (astro-ph/0611136)
- Nusser A., Silk J., 2007, arXiv, 711, arXiv:0711.1281
- Peterson J. R., Kahn S. M., Paerels F. B. S., Kaastra J. S., Tamura T., Bleeker J. A. M., Ferrigno C., Jernigan J. G., 2003, ApJ, 590, 207
- Pfrommer C., Enßlin T. A., 2004, A&A, 413, 17
- Piffaretti R., Jetzer P., Schindler S., 2003, A&A, 398, 41
- Porter, A. C., Schneider, D. P., Hoessel, J. G., 1991, AJ, 101, 1561
- Rebusco P., Churazov E., Böhringer H., Forman W., 2005, MNRAS, 359, 1041
- Rebusco P., Churazov E., Böhringer H., Forman W., 2006, MNRAS, 372, 1840
- Reimer O., Pohl M., Sreekumar P., Mattox J. R., 2003, ApJ, 588, 155
- Revnivtsev M., 2008, A&A, to be submitted
- Revnivtsev M., Churazov E., Sazonov S., Forman W., Jones C., 2007, A&A, 473, 783
- Romanowsky A. J., Kochanek C. S., 2001, ApJ, 553, 722
- Romanowsky A. J., Douglas N. G., Arnaboldi M., Kuijken K., Merrifield M. R., Napolitano N. R.; Capaccioli M., Freeman K. C., 2003, Science, 301, 1696
- Ruszkowski M., Brüggem M., Begelman M.C., 2004a, ApJ, 611, 158
- Ruszkowski M., Brüggem M., Begelman M.C., 2004b, ApJ, 615, 675
- Saglia R. P., Kronawitter A., Gerhard O., Bender R., 2000, AJ, 119, 153
- Samurović S., Danziger I. J., 2006, A&A, 458, 79
- Smith R. J., Lucey J. R., Hudson M. J., Schlegel D. J., Davies R. L., 2000, MNRAS, 313, 469
- Smith R. K., Brickhouse N. S., Liedahl D. A., Raymond J. C., 2001, ApJ, 556, L91
- Thomas J., Saglia R. P., Bender R., Thomas D., Gebhardt K., Magorrian J., Corsini E. M., Wegner G., 2007, MNRAS, 382, 657
- Vikhlinin A., Markevitch M., Murray S. S., Jones C., Forman W., Van Speybroeck L., 2005, ApJ, 628, 655
- Wu X., Tremaine S., 2006, ApJ, 643, 210